https://doi.org/10.5194/egusphere-2026-4542
Preprint. Discussion started: 16 September 2026

Acid-base chemistry controls the thermal desorption of vapors from inorganic and organic nanoparticles

Jenna DeVivo[1,2], Alexandria Stinchfield[2,3], Nirvan Bhattacharyya[2,4], Mitch Alton[5], Mingyi Wang[6], Siegfried Schobesberger[7,8,9], Liqing Hao[7], Mitchell Rogers[10], Alexander Vogel[4], Imad Zgheib[11], Natalie Burton[2,3], Clara Lietzke[8,9], Douglas M. Russell[4], Eva Sommer[12,13], Drew Gentner[10], Liine Heikkinen[14], Rainer Volkamer[8,9], Jasper Kirkby[4,12], Felipe Lopez-Hilfiker[11,15], Douglas Worsnop[5,16], Manjula Canagaratna[5], and Neil M. Donahue[1,2,3]

[1]Department of Chemistry, Carnegie Mellon University, Pittsburgh, PA, United States
[2]Center for Atmospheric Particle Studies, Carnegie Mellon University, Pittsburgh, PA, United States
[3]Department of Chemical Engineering, Carnegie Mellon University, Pittsburgh, PA, United States
[4]Institute for Atmospheric and Environmental Sciences, Goethe University Frankfurt, Frankfurt am Main, Hesse, Germany
[5]Center for Aerosol and Cloud Chemistry, Aerodyne Research Inc., Billerica, Massachusetts 01821, United States
[6]Department of the Geophysical Sciences, University of Chicago, Chicago, IL, United States
[7]Department of Technical Physics, University of Eastern Finland, PO Box 1627, 70211 Kuopio, Finland
[8]Department of Chemistry, University of Colorado Boulder, Boulder, CO, 80309, United States
[9]Cooperative Institute for Research in Environmental Sciences, Boulder, CO, 80309, United States
[10]Department of Chemical and Environmental Engineering, Yale University, New Haven, CT, United States
[11]Tofwerk AG, 3645 Thun, Switzerland
[12]CERN, European Organization for Nuclear Research, 1211 Geneva, Switzerland
[13]Faculty of Physics, University of Vienna, Strudlhofgasse 4, 1090 Vienna, Austria
[14]Department of Environmental Science and Bolin Centre for Climate Research, Stockholm University, Stockholm, Sweden.
[15]Department of Atmospheric and Climate Science, University of Washington, Seattle, 98195 WA, United States
[16]Institute for Atmospheric and Earth System Research/Physics, University of Helsinki, Helsinki, Finland

Correspondence: Neil M. Donahue (nmd@andrew.cmu.edu)

Abstract. Here, we present measurements of inorganic and organic particles using a novel instrument that simultaneously measures both acid and base compounds via temperature-programmed desorption: a Filter Inlet for Gases and AEROsols (FIGAERO) combined with a Bipolar Time-of-Flight (BTOF) mass spectrometer. We measured particles from three different sources: atomized salt solutions, aerosols formed in the CERN CLOUD chamber, and ambient aerosols from a site in New York. We find that acids and bases do not desorb at temperatures characteristic of the volatilities of their pure compounds, but rather they desorb at higher temperatures that depend on particle composition related to the entropy of the ionic condensed state, i.e. the lattice energy. For monoprotic acids, the desorption is rate-limited by a proton transfer reaction, evidenced by simultaneous desorption of the neutral acid-base pair. For ammonium sulfate ($(NH_4)_2SO_4$), we observe a step-wise release of ammonia and increase of the sulfate-to-ammonia ratio: first to triammonium sulfate hydrogen sulfate ($(NH_4)_3H(SO_4)_2$; letovicite), and then to ammonium hydrogen sulfate ($(NH_4)HSO_4$)). We find that organic acids and alkyl organosulfates also desorb at temperatures higher than those expected for their pure compounds, indicating reactive uptake. This suggests that a large fraction of organic compounds in particles may be light, ionic species, rather than fragments of low-volatility oligomers.

https://doi.org/10.5194/egusphere-2026-4542
Preprint. Discussion started: 16 September 2026

Our studies show that the FIGAERO-BTOF is a highly sensitive and versatile instrument for elucidating condensed-phase aerosol chemistry.

1 Introduction

More than half of global cloud condensation nuclei originate from particle nucleation (Gordon et al., 2017), however, the gas-phase species driving new particle formation and growth are not fully understood. This is largely because mass decreases with the cube of diameter, making smaller particles increasingly difficult to chemically characterize. As a result, the composition of freshly formed particles is often only inferred from the physical properties of aerosol (e.g. mobility diameter and number concentration) and the chemical compounds in the gas phase. This relationship is dependent on volatility (i.e. vapor pressure) and gas phase activity in equilibrium, which we will refer to as "non-reactive" condensation. Partitioning theory and frameworks such as the volatility basis set (VBS) are suitable for predicting how ultra low and extremely low volatility organic compounds (U/ELVOCs) drive nucleation and initial particle growth, followed by condensation of low volatility and semi-volatile organic compounds that grow particles to the sizes of cloud condensation nuclei (Donahue et al., 2006, 2011). In the laboratory, these predictions compare well with observed growth rates (Stolzenburg et al., 2018) and condensed-phase composition measured via thermal desorption (Lopez et al., 2025; Bhattacharyya et al., 2025).

The Filter Inlet for Gases and AEROsols (FIGAERO) is a filter-based temperature-programmed desorption inlet coupled to chemical ionization mass spectrometry (CIMS), which is sensitive to extremely small (around 10 ng) mass concentrations of organic aerosol (Lopez-Hilfiker et al., 2014). Although there is generally good agreement between experimental and parameterized volatilities for α-pinene oxidation products (Lopez et al., 2025), up to 50$\%$ of the total desorbed signal cannot be explained by partitioning according to Raoult's or Henry's Law, i.e. their mass fraction in the particles is anomalously high (Lopez-Hilfiker et al., 2015, 2016; Schobesberger et al., 2018). This signal comprises excess small, organic molecules in the particle phase that desorb at uncharacteristically high temperatures and are out of equilibrium with the gas phase. The disagreement is generally attributed to the thermal decomposition of higher order oligomers such as ROOR dimers produced from $\mathrm{RO_2}$ accretion reactions that have an internal $\mathrm{O-O}$ peroxide bond with an energy equivalent to $\sim$80 $^{\circ}\mathrm{C}$ desorption temperature (Lopez-Hilfiker et al., 2015; Lopez et al., 2025).

Beyond oligomer formation, other reactive particle-phase reactions such as acid-base chemistry contribute to particle growth, but are not yet characterized using temperature-programmed desorption. Inorganic species such as nitric acid ($\mathrm{HNO_3}$) and sulfuric acid ($\mathrm{H_2SO_4}$) have been previously reported using FIGAERO CIMS (Wang et al., 2020). However, acid desorption mechanisms are not understood and inorganic bases have not yet been measured. Consequently, temperature-programmed desorption cannot shed light on most mechanisms of new particle formation and growth because acid-base chemistry explains a large fraction of particle nucleation in nearly all regions of the present-day atmosphere (Gordon et al., 2017; Zhao et al.,

https://doi.org/10.5194/egusphere-2026-4542
Preprint. Discussion started: 16 September 2026

2024). A notable exception is ion induced isoprene-driven nucleation in pristine, high altitude environments, such as above the Amazon rainforest (Shen et al., 2024). Yet, even in remote regions, low levels of acid ($< 10^6$ cm^{-3}) enhance nucleation rates by up to two orders of magnitude compared with pure organic cases, suggesting there is a non-linear enhancement between reactive and non-reactive condensation pathways (Shen et al., 2024). FIGAERO CIMS has measured low-volatility organic oxidation products and inorganic acids from particles formed from this synergistic isoprene-acid pathway (Shen et al., 2024), but how these components interact remains an open question.

Here we present studies of the thermal desorption of inorganic and organic particles using a novel FIGAERO-BTOF, which combines a Filter Inlet for Gases and AEROsols (FIGAERO) with a Bipolar Time-of-Flight (BTOF) mass spectrometer that has rapid (0.5 s) switching between negative and positive polarities. The FIGAERO-BTOF employs up to four ion sources which are sensitive to a wide range of inorganic and organic compounds. In the negative polarity, two complementary ionization schemes, bromide (Br^-) and iodide (I^-), detect inorganic acids and oxygenated organics (as previously used with unipolar FIGAERO CIMS). In the positive polarity, acetone ($\mathrm{C_3H_7O^+}$) and benzene ($\mathrm{C_6H_6^+}$) reagents detect inorganic bases and lightly oxygenated organics. Rapid switching between polarities achieves near-simultaneous measurements of acid and base desorption.

2 Methods

2.1 FIGAERO inlet

The Filter Inlet for Gases and AEROsols (FIGAERO) is based on a temperature-programmed desorption technique coupled with chemical ionization mass spectrometry (CIMS) (Aerodyne Research Inc., Billerica, MA, USA and Tofwerk AG, Thun, Switzerland) (Lopez-Hilfiker et al., 2014). Particles are first collected on a 5.0 µm pore polytetrafluoroethylene (PTFE) filter (Millipore Sigma). After particle collection, a movable tray positions the filter in front of the ion molecule reactor (IMR) and 2.7 $\mathrm{L\,min^{-1}}$ ultrapure nitrogen flows over the filter for 1 minute, during which semi-volatile gases may partition at ambient conditions. For the remaining 14 minutes, the nitrogen is heated at a rate of approximately 10 $^\circ\mathrm{C\,min^{-1}}$ using a PID controller automated by EyeOn software (version 2.1.4.5). The filter reaches a maximum of 200 $^\circ$C, which minimizes excessive covalent bond breakage while spanning many orders of magnitude in volatility (Yang et al., 2021). The FIGAERO inlet can measure particle chemical composition at extremely low aerosol mass concentrations ($\mathrm{ng\,m^{-3}}$), or ≥ 8 nm diameter, provided there are no larger particles to interfere with the sample mass (Lopez-Hilfiker et al., 2014; Ye et al., 2019; Baalbaki et al., 2026).

There is a semi-empirical correlation between volatility and the enthalpy of vaporization (Donahue et al., 2006, 2011; Epstein et al., 2010). The temperature at which the maximum desorption rate occurs ($T_{\max}$) is related to the saturation concentration ($\log c^*$). The measured $T_{\max}$ generally increases with particle diameter and filter mass loading due to a lagged response to temperature changes (Thornton et al., 2020; Gramlich et al., 2026). Additionally, different thermocouple positions and heating rates introduce instrument-specific variations in $T_{\max}$. Calibration with known standards like polyethylene glycols are used to experimentally estimate the volatility of highly oxygenated organic molecules and other compounds for which we lack

https://doi.org/10.5194/egusphere-2026-4542
Preprint. Discussion started: 16 September 2026

authentic standards (Stark et al., 2017; Bannan et al., 2019; Ylisirniö et al., 2021, 2025). Size-dependent particle calibration curves are included in the appendix.

2.2 Bipolar time-of-flight mass spectrometer

To the best of our knowledge, the FIGAERO inlet has so far been used exclusively with unipolar time-of-flight (TOF) mass spectrometers operating with single negative reagent ions that include iodide (I^-) (Lopez-Hilfiker et al., 2014), bromide (Br^-) (Wang et al., 2021; He et al., 2021), and acetate (CH_3COO^-) ions (Lutz et al., 2019) . The FIGAERO inlet couples directly to a reduced pressure, turbulent ion molecule reactor (IMR) typically held between 100-150 mbar with a 0.019" (0.48 mm) pinhole located behind the filter.

In this study, the FIGAERO inlet couples to a Bipolar Time-of-Flight (BTOF) mass spectrometer that has rapid switching every 500 ms between positive and negative polarities, followed by ion extraction into separate time-of-flight chambers. The BTOF front-end has a Vocus AIM (Adduct Ionization Mechanism) reactor, which couples to the FIGAERO inlet using a custom polyether ether ketone (PEEK) adapter (Aerodyne, Billerica, MA, USA). The Vocus AIM reactor is a medium pressure (20-500 mbar) IMR with temperature and relative humidity control described elsewhere (Riva et al., 2024). For these experiments, the IMR was controlled at 50 mbar under dry (no additional water) conditions. The reagent ions were generated by passing ultrapure N_2 over heated permeation tubes and through Vacuum Ultra-Violet (VUV) ion sources (Ji et al., 2020). There were two VUV lamps generating either O_2^-/ $C_3H_6O^+$ ions from a pure acetone permeation tube or I^-/ $C_6H_6^+$ ions from a 1% CH_3I/C_6H_6 permeation tube. In 2 seconds, the BTOF collects mass spectra from all four ionization chemistries: oxygen (O_2^-), acetone ($C_3H_7O^+$), iodide (I^-), and benzene ($C_6H_6^+$). Alternatively, dibromomethane (CH_2Br_2) can be added to the acetone permeation tube to have Br^- chemical ionization in place of the O_2^- mode. These ion sources are used to detect acidic moieties with iodide/bromide reagent ions and basic moieties with benzene/acetone reagent ions.

2.3 Atomized salt solutions

Aqueous salt solutions were prepared from 1 $\mathrm{g\,L^{-1}}$ ammonium sulfate (Sigma, $\geq$ 99.0%), ammonium nitrate (Sigma, $\geq$ 99.0%), ammonium oxalate (Sigma, 101%), ammonium citrate tribasic (Sigma, $\geq$ 97.0%), ammonium succinate (Combi Blocks, 98%), glyoxylic acid monohydrate (Sigma, 98%), and malonic acid (Aldrich Chemical Company, Inc., 99%). For the organosulfate and sulfonic acid experiments, 25-125 mg of the following sodium salts were dissolved in 50 mL of 1 $\mathrm{g\,L^{-1}}$ ammonium sulfate/H_2O solutions: formaldehyde sodium bisulfite (Toronto Chemical Research, 98%), methyl sodium sulfate (Aldrich, 92%), sodium ethyl sulfate (Merck, 98%), butyl sodium sulfate (Toronto Research Company, 98%), sodium octyl sulfate (Merck, 95%), sodium n-decyl sulfate (Fisher Scientific, 98%), and sodium dodecyl sulfate (Merck, 98%). The solutions were atomized to create particles, which were then passed through an aerosol dryer, size-selected to 100 nm using a Differential Mobility Analyzer (TSI, Model 3082) and quantified using a water-based Condensation Particle Counter (TSI Inc., Model 3789 and 3776D). The dilution flow and particle collection time were varied to have filter mass loadings ranging from 0.05 to 1 µg, depending on the reagent ions' sensitivity to the analytes. Laboratory experiments were conducted at Aerodyne Research Inc. in Billerica, MA, USA, and Tofwerk AG in Thun, Switzerland.

https://doi.org/10.5194/egusphere-2026-4542
Preprint. Discussion started: 16 September 2026

2.4 Aerosols formed in the CLOUD chamber

In addition to the atomized samples, we include selected FIGAERO results from the Cosmics Leaving OUtdoor Droplets (CLOUD) chamber at CERN (Geneva, Switzerland), which has been described in detail elsewhere (Kirkby et al., 2011, 2016). The CLOUD chamber is a 26.1 m^{-3} stainless steel continuously-stirred tank reactor operated under ultra-clean conditions for studying *in situ* new particle formation and growth. Generally, acids are produced from gas-phase oxidation within the chamber and bases are directly injected from a gas cylinder. Hydroxyl radicals (OH) are mainly produced by photolysis of ozone in the presence of water vapor using a 5 W KrF excimer UV laser and four 200 W Hamamatsu Hg-Xe lamps. Gaseous sulfuric acid ($\mathrm{H_2SO_4}$) is produced from the oxidation of $\mathrm{SO_2}$ with OH radicals. Nitric acid ($\mathrm{HNO_3}$) is produced from the reactions of hydroxyl radicals with nitrogen dioxide ($\mathrm{NO_2}$). Nitrous acid (HONO) is produced using a reactor to continuously mix $\mathrm{H_2SO_4}$ (99%, Sigma Aldrich) and sodium nitrite ($\mathrm{NaNO_2}$, 99%, Sigma Aldrich) and then injected into the chamber to produce mixing ratios between 2 and 20 ppb HONO. A 400 W UVA LED saber ($\lambda = 385$ nm) photolyzes HONO to produce hydroxyl radicals (OH) and nitrous oxide (NO).

In the present study, seed particles were directly injected into the CLOUD chamber from an oxidation flow reactor called FLOTUS (FLow TUbe System). FLOTUS is a 60 L quartz tube with six low pressure UVC lamps, each emitting 19 W at 254 nm (Heraeus NNI 50/26XL), with gas and temperature controls independent of the CLOUD chamber.

At CLOUD, gas-phase ammonia is measured using a Tunable Infrared Laser Direct Absorption Spectroscopy (TILDAS) instrument (Aerodyne, Billerica, MA, USA) (McManus et al., 2015). Particles with diameters between 18.1 and 532.8 nm are measured using a long scanning mobility particle sizer, or lSMPS, (TSI, Model 3082) with a butanol condensation particle counter (TSI, Model 3775). An aerosol mass spectrometer (AMS) measures the total mass of non-refractory aerosol (organics, sulfate, ammonium, nitrate, and chloride) by vaporizing aerosol at very high temperature (600 °C) and using electron ionization for universal detection (Jayne et al., 2000). Aerosol acidity is estimated by the relative ratio of particulate $\mathrm{NH_4^+}$ and $\mathrm{SO_4^{2-}}$ ($\mathrm{NH_4^+/SO_4^{2-}}$) (Zhang et al., 2007). If the ratio is in a range from 1 to 2, $\mathrm{NH_4^+}$ and $\mathrm{SO_4^{2-}}$ are thermodynamically assumed to coexist in chemical forms of ammonium sulfate and ammonium hydrogen sulfate. If the ratio is in a range from 0 to 1, the two ions then coexist as ammonium bisulfate and sulfate acid (Hao et al., 2013).

2.5 Ambient Filter Collection

Ambient aerosol was analyzed from a filter collected at the City University of New York (40.82° N, 73.95° W, 89 m above sea level) during the New York City metropolitan Measurements of Emissions and TransformationS (NYC-METS) ground site intensive as part of the larger Atmospheric Emissions and Reactions Observed from Megacities to Marine Areas (AEROMMA) campaign (Hass-Mitchell et al., 2024). Sampling was conducted from August 10, 2023 21:00 EDT to August 11, 2023 05:00 EDT using a passivated stainless steel filter holder (Pall Corporation) with an upstream cyclone (URG; 2000-30EC). Aerosol was collected on a PTFE membrane filter (47 mm diameter, 1.0 µm pores, Tisch Environmental) at 100 slpm over the 8 hr period. After collection, the filter was stored in a -20 °C freezer for 10 months before a 2 mm diameter punch was taken and transported under insulated cold storage to Aerodyne Research Inc. (Billerica, MA) for subsequent FIGAERO-BTOF analysis.

https://doi.org/10.5194/egusphere-2026-4542
Preprint. Discussion started: 16 September 2026

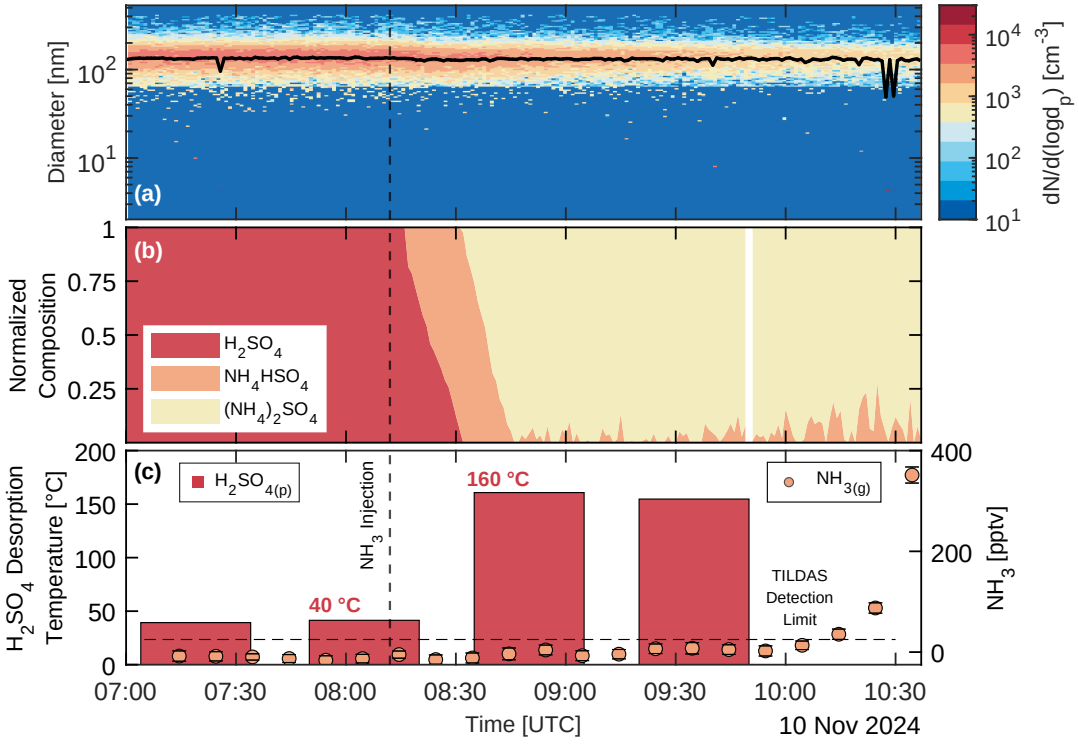

Figure 1. Sulfuric acid particles neutralized by ammonia in the CLOUD chamber (a) Particle size distribution in the CLOUD chamber measured using a long scanning mobility particle sizer (lSMPS). The particles were formed in an oxidation flow reactor (FLOTUS) from SO_2 oxidation by hydroxyl radicals to produce H_2SO_4. A batch injection of particles, with a mean diameter of 130 nm (black line), dilutes away over the course of the experiment. **(b)** Non-refractory particle composition measured by an Aerosol Mass Spectrometer (AMS). The AMS confirmed that the particles formed in FLOTUS were pure sulfuric acid (red; water not measured). After injecting ammonia (NH_3) into CLOUD (dashed vertical line), the particles were neutralized to form ammonium hydrogen sulfate (orange) initially and then ammonium sulfate (yellow). **(c)** FIGAERO I^- CIMS measures the temperature of maximum desorption rate for sulfuric acid (bars, left y-axis) where the bar width corresponds to the particle collection time. TILDAS measures gas-phase ammonia (orange circle markers, right y-axis). After ammonia injection, the H_2SO_4 desorption temperature increased from 40 to 160 °C, consistent with the neutralization observed by the AMS. However, the I^- CIMS was unipolar and only able detect sulfuric acid, with no direct measurement of ammonia in the particles. At the start of the injection, ammonia vapor is rapidly taken up by the the acidic particles. Assuming a unity accommodation coefficient, the initial condensation sink is 8.0×10^{-3} s^{-1}, about twice as large as the wall loss, 3.9×10^{-3} s^{-1}. As a result, gas-phase ammonia has large sinks to surfaces and only exceeds the TILDAS detection limit (25 pptv) about 1 hour after the injection.

3 Case studies with a unipolar FIGAERO CIMS

Vapors driving new particle formation are often assumed to have intrinsic ultra low volatility, whereas they are in fact frequently transformed into non-volatile salts in the particle phase, usually through an acid-base reaction. It is the practically zero vapor pressure of the ions, combined with an equilibrium strongly favoring the dissociated state, that results in products

https://doi.org/10.5194/egusphere-2026-4542
Preprint. Discussion started: 16 September 2026

with a sufficiently low volatility to drive nucleation. When using thermal techniques, it is important to distinguish whether the binding energy causing a species to remain on a surface is driven by a physical process (i.e. vapor pressure) or a chemical reaction. FIGAERO thermal desorption is typically treated as temperature-programmed desorption which is suitable for evaluating the strength of organic molecules adsorbed to a surface by intermolecular forces. Though the FIGAERO CIMS can measure acids, temperature-programmed desorption is ill-suited to understand their relatively high intrinsic vapor pressures. Instead, temperature-programmed reaction spectroscopy provides a better framework because it considers surface reactions that are rate-limiting to acids partitioning back to the gas-phase.

Case study* #1*: *Strong bases increase sulfuric acid desorption temperature*

Figure 1 shows changes in chemical composition when particles formed from sulfuric acid (H_2SO_4) are neutralized by ammonia (NH_3) vapor in the CLOUD chamber. Approximately 130 nm acidic particles are formed in FLOTUS from H_2SO_4/H_2O and injected as a batch of seed particles into the chamber, diluting away over time (panel 1a). The AMS observes a change in the particle chemical composition from pure sulfuric acid (red) being quickly neutralized to ammonium hydrogen sulfate (orange; NH_4HSO_4) and ammonium sulfate (yellow; $(NH_4)_2SO_4$) (Hao et al., 2013), after ammonia is added to the chamber (panel 1b). The H_2SO_4 temperature of maximum desorption (T_{max}) measured by FIGAERO I^- CIMS is plotted on the left y-axis of panel 1c, where the width of each bar corresponds to the particle collection time. After injecting ammonia, the thermograms shift dramatically hotter with the T_{max} increasing from 40 to 160 °C. This is evidence that the gas evaporated from the particles and measured in the mass spectrometer exists as different states in the particle phase, with the particle phase composition influencing the evaporation temperature. It is clear from the FIGAERO thermograms that the addition of the a small amount of ammonia has changed the particle composition making it more resistant to evaporation. However, for this experiment with the unipolar I^- FIGAERO CIMS, there was no direct measurement of any NH_3 (or NH_4^+) in the FIGAERO analysis, just the complementary measurement from the aerosol mass spectrometer (Fig 1b).

At room temperature (+25 °C), pure sulfuric acid (H_2SO_4) has a saturation vapor pressure around 1×10^{-3} Pa (Ayers et al., 1980; Kulmala and Laaksonen, 1990), making it equivalent to a semi volatile organic compound (SVOC), which contributes to aerosol growth at high concentrations, but remains volatile enough to maintain a gas-phase reservoir. In the presence of base, including weak proton acceptors like water, sulfuric acid is deprotonated to form bisulfate (HSO_4^-) and sulfate (SO_4^{2-}) ions that exist in supersaturation in the condensed state. The vapor pressure of sulfuric acid vapor over $H_2SO_4-H_2O$ solutions ranges from 10^{-6} to 10^{-9} Pa (54.1-76.0 solution wt % at +25 °C) and decreases further with increasing ionic strength down to 6.8×10^{-11} Pa for fully neutralized ammonium sulfate (Marti et al., 1997). These very low saturation vapor pressures correspond to those of extremely low volatile organic compounds (ELVOCS), which condense on all particles, including freshly nucleated ones (Donahue et al., 2026). Previous TD-PTR-CIMS (Thermal Desorption Proton Transfer Reaction CIMS) experiments have reported higher sensitivity measuring pure sulfuric acid aerosol as opposed to ammonium sulfate, indicating that the conversion of sulfate to sulfuric acid requires more energy than directly desorbing and ionizing sulfuric acid in its neutral form (Voisin et al., 2003). This result is consistent with the excess energy needed to desorb neutralized sulfate particles using

https://doi.org/10.5194/egusphere-2026-4542
Preprint. Discussion started: 16 September 2026

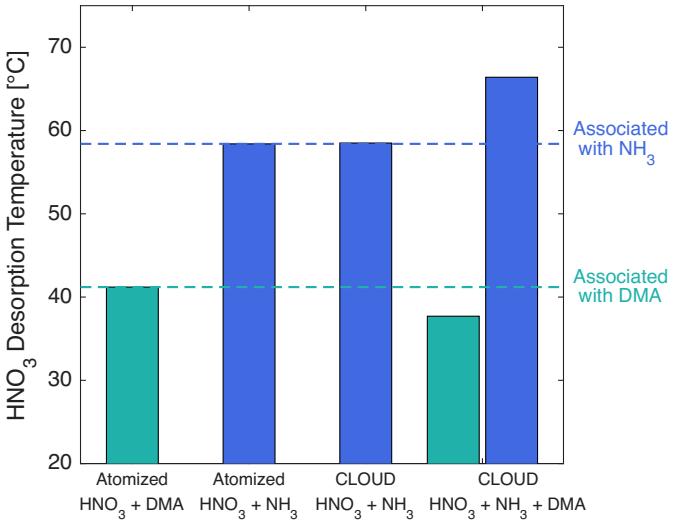

Figure 2. Nitric acid desorption temperature from aerosol with ammonia and dimethylamine. The temperature of maximum desorption (T_{max}) of nitric acid ($\mathrm{HNO_3}$) changes for aerosol containing ammonia ($\mathrm{NH_3}$) and/or dimethylamine (DMA). The first two bars come from independent calibrations using atomized solutions of dimethylammonium nitrate ($(\mathrm{CH_3})_2\mathrm{NH_2}(\mathrm{NO_3})$; teal) and ammonium nitrate ($\mathrm{NH_4NO_3}$; blue), respectively. Nitric acid from ammonium nitrate exhibits a similar desorption temperature as aerosol formed in the CLOUD chamber in the presence of sulfuric acid, nitric acid, and ammonia. In a subsequent chamber experiment that added dimethylamine (DMA), a second, lower temperature mode appears for $\mathrm{HNO_3}$ which corresponds well with the thermal desorption of dimethylammonium nitrate solution. The lower $\mathrm{HNO_3}$ desorption temperature implies the overall acid-base interaction is weaker with DMA ($\mathrm{pK_b} = 3.3$), despite it being a stronger base than ammonia ($\mathrm{pK_b} = 4.7$).

FIGAERO CIMS (Fig. 1c).

***Case study* #2:** *The effect of base size and polarizability is less predictable than base strength*

In addition to proton affinity and bond strength, acid-base interactions are governed by molecular electrostatic compatibility, where acid-base pairs with similar molecular size, polarizability, and electronegativity are energetically favored. Figure 2 compares the desorption temperature of nitric acid ($\mathrm{HNO_3}$) from aerosol containing ammonia ($\mathrm{NH_3}$) and/or dimethylamine ($(\mathrm{CH_3})_2\mathrm{NH}$). Nitric acid atomized in solutions with dimethylamine and ammonia, has respective T_{max} values of 41.2 and 58.4 °C, shown as the first two bars in Fig. 2. These laboratory measurements agree with the desorption temperatures measured from aerosol formed in the CLOUD chamber. Nitric acid that condensed with ammonia desorbs at 58.5 °C, which has been previously shown to conform with ammonium nitrate decomposition for conditions where ammonia is the only strong base (Wang et al., 2020). When dimethylamine (DMA) and $\mathrm{NH_3}$ are both present, the nitric acid thermogram becomes bimodal with the same high temperature mode at 66.4 °C and the appearance of a lower temperature mode around 37.7 °C, consistent with dimethylammonium nitrate decomposition. Despite dimethylamine ($\mathrm{p}K_\mathrm{b}$ = 3.3) being a stronger base than ammonia ($\mathrm{p}K_\mathrm{b}$ = 4.7), it requires less energy to decompose its salt with nitric acid, possibly because DMA has two methyl groups in

https://doi.org/10.5194/egusphere-2026-4542
Preprint. Discussion started: 16 September 2026

place of hydrogen atoms, which increases its polarizability and steric hindrance. These electrostatic factors affect its ionic and geometric compatibility with nitric acid and the overall stability of the lattice structure within the aerosol phase. However, this is again an indirect observation because the acids are measured by a unipolar I^- CIMS with no information about the bases. The next section investigates multivalent ionic interactions using bipolar time-of-flight mass spectrometry to directly measure the release of acid and base vapors simultaneously.

4 Bipolar FIGAERO CIMS

4.1 Inorganic acid-base interactions

The effective vapor pressure of sulfuric acid over ammonium sulfate is low because the activity includes a reactive uptake coefficient, γ^{rxn} (Lopez et al., 2025). For a monoprotic acid-base pair like ammonium nitrate, reactive uptake is driven by a single proton transfer (Donahue et al., 2025). Decomposition of the salt thus follows the reverse reaction,

$$NH_4NO_{3(p)} \rightleftharpoons HNO_{3(g)} + NH_{3(g)} \quad \text{(R1)}$$

With the FIGAERO-BTOF, simultaneous measurements of the acid and base vapors is achieved with different reagent ions as follows,

$$HNO_{3(g)} + I^-_{(g)} \rightleftharpoons (HNO_3)I^-_{(g)} \quad \text{(R2)}$$

$$NH_{3(g)} + C_3H_7O^+_{(g)} \rightleftharpoons (C_3H_6O)NH^+_{4(g)} \quad \text{(R3)}$$

In Fig. 3a, we observe near simultaneous desorption of nitric acid (38 °C) and ammonia (41 °C) from ammonium nitrate aerosol produced from atomization. The bipolar time-of-flight mass spectrometer produces the two thermograms from the same desorption cycle, though the absolute signal of the acid and base differ based on their relative sensitivity (i.e. binding energy) with the reagent ions, I^- and $C_3H_6O^+$, respectively. The similar desorption profiles for the acid and base is consistent with the rate-limiting step to evaporation being the reverse of Reaction R1 in the particle phase, a characteristic feature of temperature-programmed reaction spectroscopy.

Ammonium sulfate is seen in Fig. 3b to behave differently, since H_2SO_4 is a polyprotic acid with two labile protons. Here we observe a step-wise release of ammonia, first from ammonium sulfate ($(NH_4)_2SO_4$) to triammonium sulfate hydrogen sulfate ($(NH_4)_3H(SO_4)_2$; letovicite (Kiyoura and Urano, 1970)), and then to ammonium hydrogen sulfate (NH_4HSO_4). The ammonium-to-sulfate ratios decrease to 2.0, 1.5, and 1.0, respectively. The desorption temperatures are 78 °C, 93 °C, and 121 °C, respectively. The proposed decomposition reactions are as follows:

$$2(NH_4)_2SO_{4(p)} \leftharpoons (NH_4)_3H(SO_4)_{2(p)} + NH_{3(g)} \quad \text{(R4)}$$

$$(NH_4)_3H(SO_4)_{2(p)} \leftharpoons 2NH_4HSO_{4(p)} + NH3_{(g)} \quad \text{(R5)}$$

$$2NH_4HSO_{4(p)} \leftharpoons 2H_2SO_{4(g)} + 2NH_{3(g)} \quad \text{(R6)}$$

https://doi.org/10.5194/egusphere-2026-4542
Preprint. Discussion started: 16 September 2026

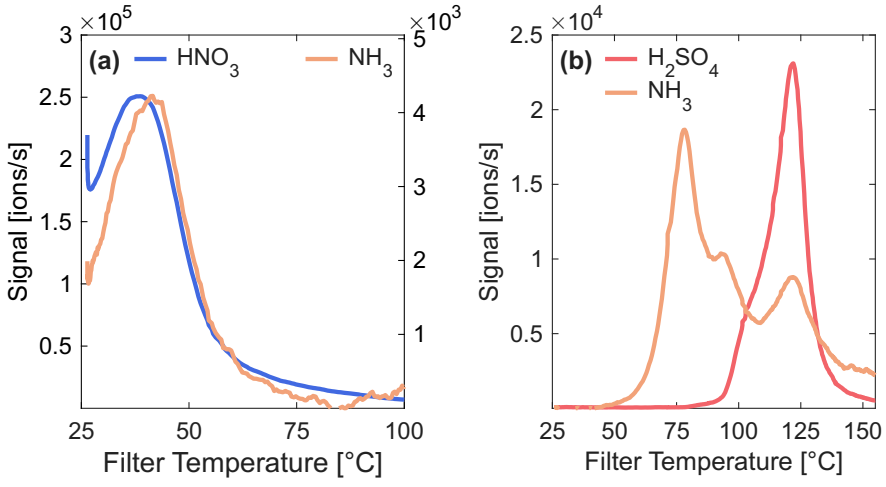

Figure 3. Ammonium nitrate and ammonium sulfate thermograms (a) Ammonium nitrate thermogram. Nitric acid (blue, left y-axis) evaporates near simultaneously with ammonia (orange, right y-axis) at around 40 °C. **(b)** Ammonium sulfate thermogram. Ammonia exhibits three modes of desorption with maxima at 78, 93, and 121 °C. Sulfuric acid (red) begins desorbing around the first ammonia mode (Fig. A1), but has only a single, resolvable maximum at 121 °C, coincident with the final NH_3 peak.

Ammonium sulfate decomposition has been previously studied in bulk solution using thermogravimetric analysis (TGA). Those studies report two distinct modes of ammonium sulfate decomposition, with the lower temperature mode liberating ammonia alone (Dixon, 1944). However, there is still uncertainty about the intermediate products. Depending on the rate of heating, ammonium sulfate may decompose through either letovicite (deammoniation) or ammonium hydrogen sulfate (dehydration), followed by further, high temperature ($>$ 250 °C) degradation to products like pyrosulfate, sulfamic acid, and other gases (Erdey et al., 1964; Halstead, 1970; Kiyoura and Urano, 1970; Zelenková and Slovák, 2022; Kaniewski et al., 2023). We resolve three modes using FIGAERO CIMS in this study, possibly because the slower heating rate increases peak prominence for the letovicite (second) mode or promotes dehydration reactions rather than thermal ones. Alternatively, the decomposition of ammonium sulfate to letovicite involves crystallization that may be promoted by increased supersaturation and efflorescence in the aerosol phase compared to the bulk.

By mass, most of the sulfuric acid desorbs at the highest temperature mode associated with ammonium hydrogen sulfate decomposition. This explains why in Fig. 1c the sulfuric acid desorption temperature from partially and fully neutralized aerosol appears unchanged. If sulfate exists, it is stepwise converted to bisulfate in the particle phase, a process we can only indirectly observe through the release of ammonia. The H_2SO_4 T_{max} for fully neutralized aerosol in Fig. 1c is much higher than the atomized sample in Fig. 3b, likely owing to differences in mass loadings, heating rates, and thermocouple positions. While calibration can correct for these differences, the ammonia signal can provide a definitive marker of neutralized ammonium sulfate without needing a reference. Figure A1 demonstrates that the aerosol formation method (i.e. atomization vs. condensation) does not significantly affect the results. The relative intensity of the ammonia modes could be an indicator of the degree of neu-

https://doi.org/10.5194/egusphere-2026-4542
Preprint. Discussion started: 16 September 2026

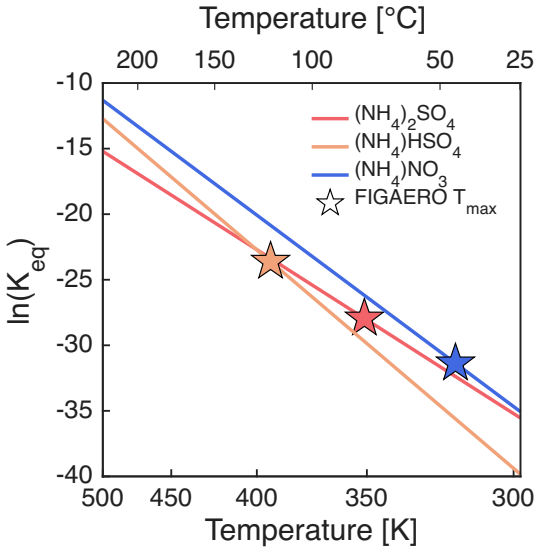

Figure 4. Salt dissociation as a function of temperature. Van 't Hoff plot for ammonium sulfate (red), ammonium hydrogen sulfate (orange), and ammonium nitrate (blue) decomposition. The slope of each line corresponds to the change in enthalpy ΔH as a function of inverse temperature. The temperature is plotted as 1/T with labels indicating T in units of Kelvin and Celsius on the bottom and top x-axis, respectively. The FIGAERO $T_{\max}$ values for the ammonia signal of each decomposition reaction are plotted as stars.

tralization. Alternatively, the ratio of total NH_3-to-H_2SO_4 could estimate pH. The latter is useful since reaction spectroscopy does not necessarily have uniform distributions and thus multi-modal thermograms may be best treated by integration across the total time, as opposed to integrating non-uniform modes.

The shape of the sulfuric acid thermogram is non-Gaussian, exhibiting a low temperature shoulder around the temperature associated with letovicite decomposition. On a logarithmic scale (Fig. A1), sulfuric acid first appears around the first maximum of the ammonia mode, indicating other minor chemical reactions may be occurring, or that the reactions identified are not in equilibrium. Smaller particles with lower heat capacity and consequently faster internal heating may explain the non-uniform sulfuric acid profile. Core-shell morphology formed from the dehydration and crystallization process could also delay diffusion of heat into the particle and evaporation of chemical species out of the core.

4.2 Lattice energy

Coincident evaporation of H_2SO_4 and NH_3 at 121 °C is evidence that a chemical process, specifically a proton transfer, is the energetically rate-limiting step to desorption; in essence, reactive uptake in reverse. To study the reaction kinetics, we compared our results with the thermodynamics of ammonium nitrate, ammonium hydrogen sulfate, and ammonium sulfate formation reactions (Gmitro and Vermuelen, 1963; Scott and Cattell, 1979; Rumble, 2025). We do not observe a correlation between the temperature of maximum desorption ($T_{\max}$) and the enthalpy of reaction (ΔH_{rxn}), the entropy of reaction (ΔS_{rxn}), or the acid dissociation constant ($\mathrm{p}K_{\mathrm{a}}$) (Table A4). This contrasts non-reactive condensation where there is a linear relationship between

https://doi.org/10.5194/egusphere-2026-4542
Preprint. Discussion started: 16 September 2026

the enthalpy of vaporization (ΔH_{vap}) and T_{max} (Bannan et al., 2019; Ylisirniö et al., 2021). Instead, the van 't Hoff plot in Fig. 4 demonstrates a dependence on the net change in Gibbs free energy of reaction, ΔG_{rxn}, which includes the entropic change, ΔS_{rxn}, during evaporation. ΔS_{rxn} is often estimated by the entropy related to the overall change in phase state (Trouton's rule); however, for highly ordered condensed states like the salt crystals, lattice energy can meaningfully contribute to the entropy term of Gibbs free energy. Using ΔG_{rxn}, we calculate the equilibrium constant, K_{eq}, of salt formation and decomposition as a function of temperature:

$$K_{eq} = e^{\frac{-\Delta G_{rxn}}{RT}} \tag{1}$$

The temperature dependence is expressed as the van 't Hoff equation:

$$\ln(K_{\mathrm{eq}}) = -\frac{\Delta H^o}{R}\frac{1}{T} + \frac{\Delta S^o}{R} \tag{2}$$

The van 't Hoff plot in Fig. 4 spans the typical temperature range of FIGAERO thermal desorption (298-500 K, or ~25-200 °C). At 298 K (+25 °C), ammonium nitrate and ammonium sulfate have similar equilibrium constants (Table A4). According to Eq. (2), the slope of the equilibrium constant is driven by changes in enthalpy and the y-intercept by entropy. As temperature increases, the NH_4NO_3 equilibrium constant increases faster than for the sulfate salts, consistent with it desorbing at a lower temperature. The stars mark the T_{max} of the ammonia mode associated with each salt decomposition, appearing in order of the experimental observations. The ammonium hydrogen sulfate (orange) curve lies above that for ammonium sulfate (red) beyond where we observe ammonium hydrogen sulfate decomposition. The crossover of ammonium sulfate and ammonium hydrogen sulfate curves corresponds to the T_{max} of ammonium hydrogen sulfate, consistent with the final decomposition step being favored above 400 K (+127 °C). Altogether, these trends indicate that neither enthalpy nor entropy alone can explain acid-base desorption because the internal lattice arrangement involves covalent bond reactions (i.e. proton transfer) in addition to intermolecular forces.

4.3 Organic acid-base reactions

4.3.1 Organosulfates

Organosulfates (OS) contain sulfate ($-OSO_3H$) functionalities with a carbon backbone ($-R$) attached at the sulfate ester. They can thus act like an Brønsted Lowry acid, where the acid dissociation constant (pK_a) is largely modulated by the structure of $-R$ and nearby functional groups. Isoprene and monoterpene derived organosulfates are estimated to have very low pK_a values between -4.5 and -2.4, similar to sulfuric acid (Hyttinen et al., 2020). Due to challenges measuring organosulfates, their formation mechanisms remain disputed (Brüggemann et al., 2020), with disagreement whether OS predominantly form in the aqueous condensed phase or are formed in the gas phase and condense via a chemical reaction. As a result, it is unclear if reactive or non-reactive processes drive OS and OS-precursors into the condensed phase.

https://doi.org/10.5194/egusphere-2026-4542
Preprint. Discussion started: 16 September 2026

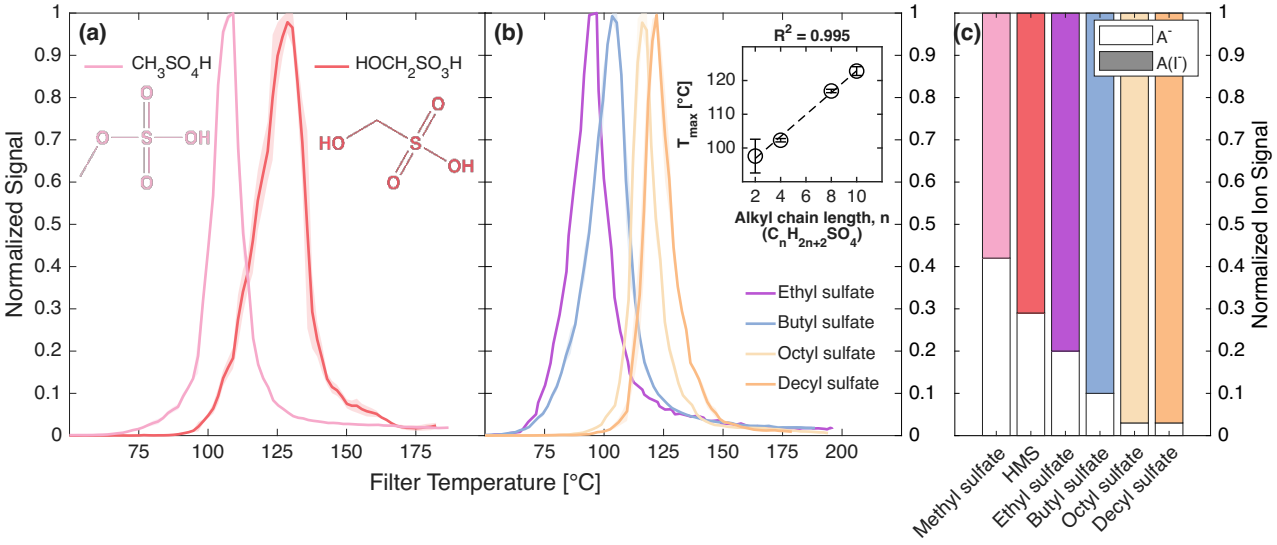

Figure 5. Thermograms for C_1 (a) and C_2-C_{10} (b) organosulfur compounds. In panel **(a)**, two structural isomers, methyl bisulfate (pink) and hydroxymethanesulfonic acid (HMS; red), desorb at high temperatures ($>$ 100 °C) but about 20 °C apart. In panel (**b**), ethyl (purple), butyl (blue), octyl (yellow), and decyl (orange) sulfate desorb at sequentially higher temperatures. $T_{\max}$ increases linearly with alkyl chain length, n, in $C_nH_{2n+2}SO_4$ (R^2 = 0.995). Panel **(c)** shows the normalized fraction of each organosulfur species detected in the deprotonated form (empty bar) and as an adduct with I^- (colored bar). A larger fraction of the smaller organosulfur molecules are deprotonated.

Particulate organosulfates have been previously reported using FIGAERO CIMS (Le Breton et al., 2018; Ye et al., 2021; Siegel et al., 2021; Cai et al., 2023) with the majority of measurements occurring in Chinese megacities where aerosol mass loading and anthropogenic sulfur sources are high. Given limited measurements, the global prevalence of organosulfates in ambient aerosol is uncertain (Brüggemann et al., 2020), a problem further compounded by OS-related measurement uncertainties using different techniques. For time-of-flight mass spectrometers with resolutions ranging from $5{,}000 \leq \mathrm{m}/\Delta\mathrm{m} \leq 10{,}000$, organosulfates (CHOS) and pure organic (CHO) species are difficult to resolve (the difference in exact mass between two oxygen atoms and one sulfur atom being 0.017758 Th). Thermal desorption techniques like FIGAERO can potentially use $T_{\max}$ to distinguish between pure organic compounds (condensing via strong intermolecular forces) and organosulfates (acting more like sulfuric acid requiring a proton transfer). However, this is predicated on organosulfates withstanding thermal decomposition at the sulfate ester (Lopez-Hilfiker et al., 2016; D'Ambro et al., 2019) and being efficiently detected using chemical ionization mass spectrometry.

To study the desorption behavior of organosulfates, we atomized a homologous sequence of alkyl organosulfates. The organosulfates were obtained as sodium salts (e.g. $C_4H_{10}NaSO_4$) and dissolved in water to create an aqueous solution. When atomized in water alone, we did not observe signal with any ionization mode, likely because there were insufficient protons available to neutralize the organosulfates such that they could not partition back to the gas phase. Therefore, each organosulfate was mixed with 1 g/L ammonium sulfate solution to provide a H^+ source. The results are summarized in Table 1.

https://doi.org/10.5194/egusphere-2026-4542
Preprint. Discussion started: 16 September 2026

Table 1. T_{max} for alkyl organosulfate standards. Each sodium salt was mixed with 1 g L^{-1} ammonium sulfate solution to provide a source of H^+ ions. The effective vapor pressures (P^*_{expt}) were calculated using the experimental T_{max} values (Table A2). The predicted vapor pressures (P_{pred}) were calculated using the group contribution-assisted graph convolutional neural network (GC^2NN) model (Accessed: https://multiphasekinetics.de/pvap; (Krüger et al., 2025)). The dodecyl sodium sulfate sample was run at as single experiment at Tofwerk AG and is excluded from Fig. 6 because it requires an independent calibration.

Chemical name	Acid formula	M_w [g mol^{-1}]	T_{max} [°C]	P^*_{expt} [Pa]	P_{pred} [Pa]
Formaldehyde sodium bisulfite	$HOCH_2SO_3$	111.10	126.5 ± 1.4	3.2×10^{-11}	8.25×10^{-2}
Methyl sodium sulfate	CH_3SO_4	111.10	106.9 ± 0.1	8.9×10^{-10}	1.06
Ethyl sodium sulfate	$C_2H_6SO_4$	126.13	97.6 ± 5.0	4.3×10^{-9}	1.33×10^{-1}
Butyl sodium sulfate	$C_4H_{10}SO_4$	154.18	102.3 ± 0.5	1.9×10^{-9}	3.96×10^{-3}
Octyl sodium sulfate	$C_8H_{18}SO_4$	210.29	116.9 ± 0.5	1.6×10^{-10}	2.80×10^{-4}
N-decyl sodium sulfate	$C_{10}H_{22}SO_4$	238.34	122.8 ± 1.3	5.9×10^{-11}	1.43×10^{-4}
Dodecyl sodium sulfate	$C_{12}H_{26}SO_4$	266.40	140 (n=1)		2.64×10^{-5}

Figure 5a shows the thermogram for two single carbon organosulfur species: hydroxymethanesulfonic acid ($HOCH_2SO_3H$) and methyl bisulfate (CH_4SO_4). Despite having the same molecular mass, the T_{max} of the structural isomers differs by 20 °C. In the presence of ammonium sulfate, hydroxymethanesulfonic acid desorbs at a higher temperature, around 127 °C. It is a strong acid, similar to methanesulfonic or sulfuric acid, and so dissociates completely in aqueous solutions. Methyl sulfate, also a strong acid, desorbs at a lower temperature around 107 °C. Hydroxymethanesulfonic acid may desorb at a higher temperature because it has an additional $-OH$ functional group that can hydrogen-bond with neighboring molecules. Hydroxymethanesulfonic acid has been previously observed in ambient aerosol and is an important S(IV) acid formed via aqueous reactions of SO_2 and formaldehyde during cloud processing (Dovrou et al., 2019). Other small organosulfur species like methanesulfonic acid, an oxidation product of dimethylsulfide, are abundant in marine aerosol and have been observed desorbing at high temperatures (> 100 °C) in FIGAERO CIMS (Cai et al., 2023). This class of molecules - methyl bisulfate (CH_3SO_4H), methanesulfonic acid (CH_3SO_3H), and hydroxymethanesulfonic acid ($HOCH_2SO_3H$) - represent an important class of organosulfates and sulfonates behaving largely like inorganic sulfur with variation attributed to H-bonding or intermolecular forces unique to each molecule.

Figure 5b shows that alkyl sulfates with more than one carbon atom also desorb at relatively high temperatures (> 98 °C), with desorption temperature increasing with the number of carbon atoms. The T_{max} values are plotted versus the alkyl chain length, n, for $C_nH_{2n+2}SO_4$ in the embedded plot of Fig. 5b. There is a linear relationship ($R^2 = 0.995$) between alkyl chain length and desorption temperature, likely because chain length affects the internal structure of the condensed phase. In addition to having more surface interactions and van der Waals forces, the sulfate series is special in that the alkyl chain is attached to a hydrophobic tail off of the hydrophilic sulfate group. With increasing chain length, the hydrophobic tail is more effective

https://doi.org/10.5194/egusphere-2026-4542
Preprint. Discussion started: 16 September 2026

at forming internal structures such as micelles based on hydrophobicity, which affects the energy required to overcome the entropy-favored condensed state and form the neutral sulfate ester.

All organosulfur species were measured in the negative I^- mode appearing in the deprotonated (A^-) and adduct (AI^-) form. Larger molecules had a larger fraction of the total signal detected as clusters with I^-, as opposed to deprotonated ions. This trend may be caused by a decrease in acidity with a larger alkyl chain that increases the acidic proton bond strength. Alternatively, larger molecules may form stronger clusters with I^- ions that have more diffuse electronegativity (i.e. more effective orbital overlap).

Due to a lack of experimental vapor pressure for low-volatility, atmospheric compounds, structure activity relationships (SARs) are used to estimate volatility (Hilal et al., 2003; Nannoolal et al., 2008; Pankow and Asher, 2008; Compernolle et al., 2011). Yet, even for well-characterized compounds like α-pinene oxidation products, SAR models can underestimate volatility because they do not consider intramolecular forces (Kurtén et al., 2016). For smaller alkenes with multi-functional but well-known product distributions, significant differences between observed partitioning and SAR models have been attributed to increased intramolecular steric effects (Longnecker et al., 2025). Moreover, compounds with more exotic functional groups (e.g. sulfates, nitrates, peroxy acyl nitrates) are excluded or not well characterized by most SAR models. Thermodynamic models like COSMO*therm* can estimate the volatility of isoprene and monoterpene-derived organosulfates, but generally overpredict salting out effects (i.e. decreased organic solubility) (Toivola et al., 2017) and require quantum chemical and statistical calculations which are more computationally expensive than a typical SAR model (Hyttinen et al., 2020). New machine learning models like the group-contribution-assisted graph convolutional neural networks (GC^2NN) have large training datasets with greater diversity of compounds, however, organosulfates still represent $< 1\%$ of the data set (Krüger et al., 2025). Nevertheless, there is a good agreement for isoprene-derived organosulfate vapor pressures using the COSMOtherm and GC^2NN models (Hyttinen et al., 2020; Krüger et al., 2025). Table 1 compares the experimental vapor pressure of the organosulfates in this study with predicted vapor pressures from the GC^2NN model. Overall, there is a poor agreement, likely because the strength of ion-ion interactions differs in our study using ammonium sulfate compared to the pure substance. The experimental data and model do show similar overall trends. The model predicts methyl sulfate to be approximately an order of magnitude more volatile than hydroxymethanesulfonic acid, consistent with our observations. Likewise, the predicted vapor pressures decrease with increasing chain length for the alkyl organosulfates. While the measured organosulfate vapor pressures are likely biased lower due to the presence of ammonium, this comparison highlights the need for a parameterization that includes acid-base interactions as pure organosulfate aerosol is unlikely.

Thermal desorption instruments typically report smaller fractions of organosulfates than offline methods using liquid chromatography. Offline chromatography techniques using ultra-high resolution Orbitrap analysis estimate that organosulfates contribute up to 30 % of organic aerosol mass (Ma et al., 2025), but with a sensitivity bias towards detecting acidic species. Offline techniques may have surface reactions on the filter after sampling, potentially enhancing organosulfates (Brüggemann et al., 2021). Alternatively, semi-online thermal techniques like FIGAERO CIMS may not accurately measure organosulfates. One explanation is that the organosulfates are desorbing at very high temperatures ($> 200\,^\circ C$) beyond the maximum temperature of the filter. However, the latter hypothesis is not supported by our results, which show that very acidic organosulfates ($pK_a \approx -3$)

https://doi.org/10.5194/egusphere-2026-4542
Preprint. Discussion started: 16 September 2026

Table 2. Comparison of FIGAERO-derived experimental vapor pressures for organic acids compared with literature values. Aerosol particles were produced by atomization of [a]ammonium salts or [b]the pure substance mixed with ammonium sulfate. Note that we are reporting the T_{max} of the neutral organic acids, but they almost certainly existed in the ionic form (e.g. glyoxylate → glyoxylic acid). The T_{max} is used to calculate an experimental effective vapor pressure (P^*_{expt}) and volatility ($\log c^*_{expt}$). Malonic acid desorbed with ammonia but had a wide thermogram, and so T_{max} could not be determined. Literature vapor pressures (P^*_{lit}) are from NIH PubChem (accessed 8 April 2026), and include primary sources for oxalic acid (Bernales, 1981), malonic acid (Bilde et al., 2003), and succinic acid (Yaws, 1994). Good agreement between T_{max} and literature volatility ($\log c^*_{expt}$) is defined by a difference in literature and experimental saturation mass concentrations (C^*) less than one order of magnitude (Lopez et al., 2025). Literature acid dissociation constants (pK_a) are retrieved from NIH PubChem; they include primary sources for glyoxylic acid (Lange and Dean, 1998), oxalic acid (Edwards and Clayton, 1981), malonic acid (Kortüm et al., 1961), succinic acid (Dean, 1987), and citric acid (Serjeant and Dempsey, 1979).

Chemical name	Formula	T_{max} [°C]	P^*_{expt} [Pa]	P^*_{lit} [Pa]	$\log c^*_{expt}$	$\log c^*_{lit}$	$T_{max} - \log c^*_{lit}$ relation?	pK^1_a	pK^2_a
Glyoxylic acid[a]	$C_2H_2O_3$	50	1.7×10^{-4}	140	0.70	6.6	no	3.3	
Oxalic acid[a]	$C_2H_2O_4$	40	1.0×10^{-3}	0.03	1.6	3.0	no	1.5	4.4
Malonic acid[b]	$C_3H_4O_4$	n/a	n/a	3.6×10^{-4}	n/a	1.2	no	2.8	5.7
Succinic acid[a]	$C_4H_6O_4$	42	6.1×10^{-4}	2.5×10^{-5}	1.5	0.076	no	4.2	5.6
Citric acid[a]	$C_6H_8O_7$	92	8.9×10^{-8}	4.9×10^{-7}	-2.2	-1.4	yes	2.8	4.4

with one to ten carbon atoms desorb between approximately 100 to 125 °C, a typical range for FIGAERO thermal desorption. A second possibility is that the temperature ramp is too harsh, causing the organosulfate to decompose between the C−O bond of the sulfate ester. If alkyl sulfates decompose, the organic portion would not be highly oxygenated, but rather an alkene or alkenol, which could be detected in the positive mode but is not observed. For these selected species, there is no evidence that thermal decomposition has any major role in explaining a potential source of "missing" organosulfur compounds. It is possible that more highly oxygenated organosulfates behave differently due to other intermolecular forces. Additionally, heating in the presence of other reactive species (e.g. peroxides) or oxidizing agents (HNO_3) may split the ester bond and cause other degradation pathways which are not captured here. Though the discrepancy in reported fraction of organosulfates between online and offline measurements is unresolved, Fig. 5 demonstrates that the FIGAERO-BTOF can measure organosulfates and their effective vapor pressure in different states to better understand their role in atmospheric aerosol.

4.3.2 Organic acids

Organic acids, though typically less acidic than those with sulfur heteroatoms, have relatively low acid dissociation constants (pK_a) and are abundant in the atmosphere. This is especially true for small, polar organics and dicarboxylic acids like oxalic acid ($C_2H_2O_4$) (Chebbi and Carlier, 1996). Carboxylic acids are formed via gas-phase oxidation and via multi-phase chemistry in droplets, which break down organics into smaller, acidic fragments (Blando and Turpin, 2000; Warneck, 2003; Crahan et al., 2004; Lee et al., 2012). Organic acids affect aerosol physical properties (e.g. mass transfer, hygroscopicity, cloud condensation nuclei activity) as well as chemical properties (e.g. heterogeneous reactivity) properties. In addition to having strong ionic

https://doi.org/10.5194/egusphere-2026-4542
Preprint. Discussion started: 16 September 2026

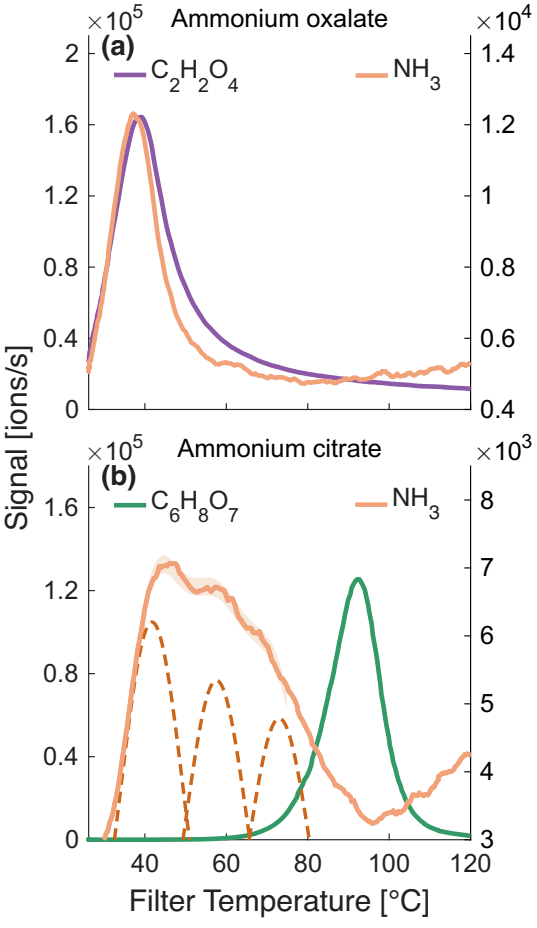

Figure 6. Ammonium oxalate and ammonium citrate thermograms. Acids are ionized by I^- and plotted on the left y-axis. Bases are ionized by $C_3H_7O^+$ and plotted on the right y-axis. **(a)** For ammonium oxalate, a proton transfer reaction is rate limiting to oxalic acid (purple) and ammonia (orange) evaporation which occur near simultaneously. **(b)** For ammonium citrate, we observe a wide band of ammonia desorption which can be fitted by three Gaussian distributions (dashed curves) corresponding to the three proton sites on citric acid (green). The neutral acid desorbs at a high temperature after ammonia has evaporated, indicating that while an ammonia-releasing reaction occurred, it was not limiting the rate of acid desorption, i.e. citric acid remained on the filter.

https://doi.org/10.5194/egusphere-2026-4542
Preprint. Discussion started: 16 September 2026

bonds and ion-dipole interactions with other organics, organic acids may also interact with inorganic salts (McNeill et al., 2007). For example, oxalic acid creates a hard coating on di-valent salts, strongly reducing hygroscopicity (Drozd et al., 2014).

Organic salts have previously been measured by chemical ionization mass spectrometry (CIMS), appearing in the neutral acid form (McNeill et al., 2007). They appear out of equilibrium with the gas phase activity because the condensed form is the conjugate base (e.g. oxalate) (McNeill et al., 2007). A previous FIGAERO $C_2H_3O_2^-$ CIMS study found that carboxylic acids obey Raoult's law under low sulfate mass concentrations ($[SO_4^{2-}] < 0.4\ \mu g\ m^{-3}$), but the relationship fails at higher sulfate conditions, suggesting gas-particle equilibrium is disrupted by conditions associated with acidic aerosol (Lutz et al., 2019). Moreover, an instrumental comparison using FIGAERO I^- CIMS derived T_{max}-derived volatilities for $C_2H_2O_3$ and $C_3H_2O_3$ that were inexplicably higher than those based on structure, leading the authors to conclude that they could not exist in the particle phase and must be resulting from fragmentation of larger species (Du et al., 2022).

Here, the FIGAERO-BTOF provides crucial additional information compared with previous studies to understand the desorption temperatures of organic acids and their partitioning with the gas phase. Figure 6a shows the thermal desorption spectrum for ammonium oxalate (neutral acid $pK_a = 1.5$). We observe near-simultaneous desorption of neutral oxalic acid and ammonia between 37-40 °C, analogous to ammonium nitrate (Fig. 3a). The ammonia signal indicates an acid-base reaction occurred, transforming the conjugate base, oxalate, to oxalic acid. In the neutral forms, both oxalic acid and ammonia are volatile and out of equilibrium with (i.e. greatly in excess of) their respective gas phase activities, resulting in rapid desorption.

Figure 6b shows different behavior for ammonium citrate ($pK_a = 2.8$). We do not observe simultaneous release of ammonia and citric acid. Instead, there is broad desorption of ammonia between 40-80 °C but citric acid has a much higher T_{max} of 92 °C, after almost all ammonia has evaporated. The data show at least two rate-limiting steps for desorption. First, a proton transfer reaction produces both neutral ammonia and citric acid. This reaction marks the rate-limiting step to desorption for ammonia, which is volatile above room temperature. The broad desorption of ammonia is consistent with three poorly resolved peaks corresponding to multiple reactions with citric acid which is a triprotic acid. Consequently, it may liberate ammonia on a mole-to-mole basis at different temperatures depending on the acidic site of the molecule.

In contrast to ammonia, citric acid has low volatility even in its neutral form and remains bound by intermolecular forces, desorbing at 92 °C. The experimental $\log c^*$ (-2.2) and literature value (-1.4) are within the typical uncertainty associated with the FIGAERO (Lopez et al., 2025), and are consistent with citric acid evaporating as a function of vapor pressure. The experimental T_{max} for citric acid is also consistent with previous results (Stark et al., 2017; Ye et al., 2019), taking into account differences in mass loading, thermocouple placement, and heating rate. We also observe aconitic acid ($C_6H_6O_6$), the tricarboxylic citric acid anhydride, desorbing at a slightly higher temperature than citric acid. Aconitic acid has been proposed as an intermediate decomposition product eventually forming CO_2, CO, and H_2O (Stark et al., 2017) in the gas phase. These gaseous decomposition products were not measured in this study, however, they have previously been observed desorbing at high temperatures ($100 \leq T_{max} \leq 200$ °C) (Stark et al., 2017) and so are likely not related with the ammonia desorption.

Table 2 summarizes the T_{max} for all organic acid samples. Glyoxylic, oxalic, and malonic acids behave similarly, desorbing simultaneously with ammonia at temperatures higher than those predicted from their pure vapor pressure. This indicates that proton transfer is the rate-limiting step for desorption of the small organic acids. The larger and more oxygenated organic acids,

https://doi.org/10.5194/egusphere-2026-4542
Preprint. Discussion started: 16 September 2026

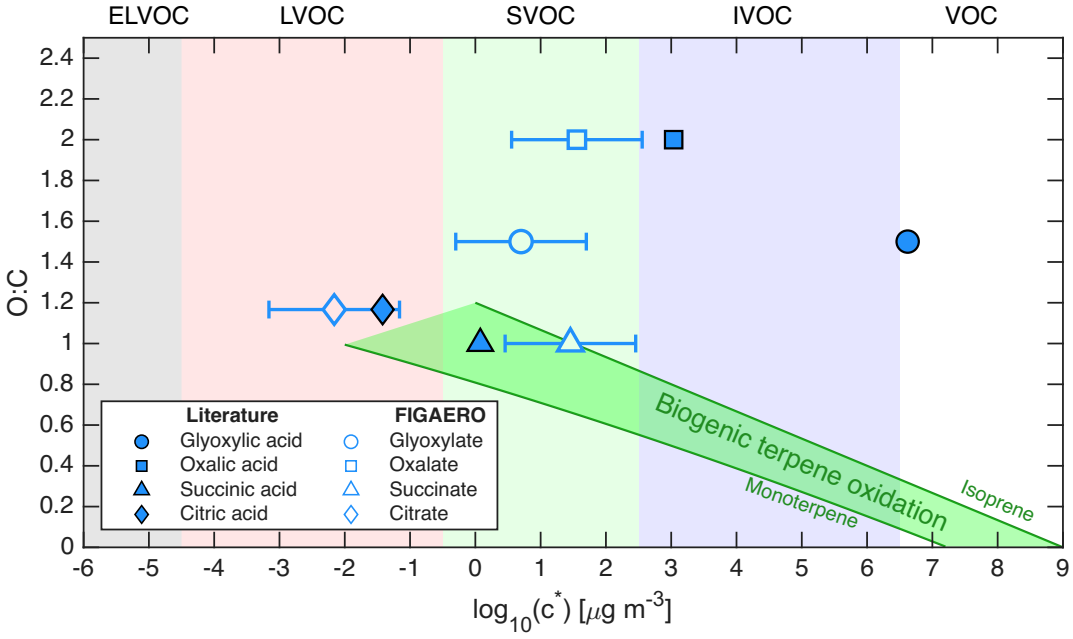

Figure 7. Two-dimensional volatility basis set for organic acids and their conjugate bases. Experimental volatilities calculated from $T_{\max}$ are shown as empty markers for glyoxylate (circle), oxalate (square), succinate (triangle), and citrate (diamond) ions. Error bars indicate one order of magnitude uncertainty in the log saturation concentration, $\log c^*$ (Lopez et al., 2025). Filled markers show the corresponding organic acids with volatility calculated from the literature vapor pressures (Bernales, 1981; Bilde et al., 2003; Yaws, 1994). The shaded backgrounds are volatility classes including volatile organic compounds (VOC; white), intermediate volatility organic compounds (IVOC; blue), semi-volatile organic compounds (SVOC; green), low volatility organic compounds (LVOC; red), and extremely low volatility organic compounds (ELVOC; grey). The brighter green on top represents the region occupied by biogenic terpene oxidation products at 25 °C, where the upper and lower bounds represent isoprene and α-pinene autoxidation products, respectively, reproduced from Schervish et al. (2024). This shows that small deprotonated acids have similar volatility as oxygenated organic molecules from terpenoids, but acids have similar or higher oxygen-to-carbon ratio (O:C). The FIGAERO signal for the smallest organics (glyoxylate and oxalate) lie out of equilibrium with their conjugate acids indicating they were formed by reactive processes in the particle phase. Succinic acid and its conjugate base are both semi-volatile organic compounds and the measured volatility based on desorption temperature is less than the literature value. Citric acid is a low volatility organic compound desorbing as a function of its vapor pressure, though a prior chemical transformation occurred that did not lead to desorption.

https://doi.org/10.5194/egusphere-2026-4542
Preprint. Discussion started: 16 September 2026

succinic and citric acid, show more consistent $T_{\max} - \log c^{\circ}$ agreement, though there is larger uncertainty for succinic acid which has an experimental vapor pressure lower than predicted. They were the least volatile organic acids studied, behaving like semi-volatile and low volatility organic compounds, respectively, at 25 °C, though likely still requiring available protons to become neutralized. The organic acids are plotted in the two-dimensional volatility basis set (2D-VBS) in Fig. 7, along with a shaded green region representing isoprene (upper bound) and α-pinene (lower bound) autoxidation products that have similar volatilities and relative oxygen content (Donahue et al., 2011; Schervish et al., 2024). The small organic acids occupy the same volatility space as highly oxygenated isoprene molecules, but do not originate from thermal decomposition. Aerosol particles from isoprene and α-pinene chamber experiments, chemically characterized using FIGAERO CIMS, show a high fraction of small, low volatility organics, which are generally attributed to thermal decomposition (Lopez-Hilfiker et al., 2016; Lopez et al., 2025). Our measurements indicate rather that some of these light carbon species are organic acids whose low volatility results from reactive uptake from the vapor phase to form ionic salts in the particles.

4.4 Multicomponent chemical systems

4.4.1 Mixtures of ammonium nitrate and ammonium sulfate

For the single acid-base systems considered so far, there are a limited number of reaction steps and sufficient mass to resolve the unique $T_{\max}$ values associated with the Gibbs free energy of reaction. To evaluate the desorption method for more complex chemical systems, Fig. 8 shows thermal desorption profiles for atomized mixtures of ammonium nitrate, ammonium sulfate, and water, with increasing sulfate fraction from panel a to d. In the top panel, pure ammonium nitrate aerosol has near-simultaneous desorption of nitric acid and ammonia, as previously seen in Fig. 3a. The bottom panel shows the thermograms for pure ammonium sulfate particles as shown in Fig. 3b. There is a small amount of nitric acid contamination (multiplied by 20) peaking at the ammonium bisulfate decomposition temperature and which is not depleted at higher temperatures. Though this could be nitrate contamination within the particles, the elevated signal at the end of the temperature ramp implies a near-constant source of nitric acid, perhaps from surfaces between the filter and entrance to the mass spectrometer.

The two middle panels shown atomized mixtures of ammonium sulfate (AS) and ammonium nitrate (AN) where one is in excess of the other. Panel 8b has an ammonium sulfate to ammonium nitrate ratio (AS:AN) of 1:2. The thermograms share distinctive features with the acid thermogram appearing similarly to that of the pure ammonium nitrate and ammonium sulfate cases. The ammonia thermogram has local maxima for every decomposition reaction (vertical dashed lines) with a long tail with decreasing intensity at high temperatures. Panel 8c has an excess of sulfate (AS:AN = 3:1) and appears less like a hybrid of the pure ammonium nitrate and ammonium sulfate cases. There is relatively low nitric acid signal (multiplied by 20) spread out in a bimodal distribution. The first nitric acid mode appears without ammonia, likely due to insufficient signal-to-noise in the positive channel where benzene/acetone ions have lower sensitivity to ammonia, compared to iodide and nitric acid adducts. The second maximum of the nitric acid thermogram appears with ammonia at the temperature of ammonium sulfate decomposition. Ammonia likely has sufficient signal at this temperature due to proton transfer reactions with sulfuric acid. The sulfuric acid thermogram appears remarkably similar to panel 8d, implying ammonium bisulfate decomposition is still a major

https://doi.org/10.5194/egusphere-2026-4542
Preprint. Discussion started: 16 September 2026

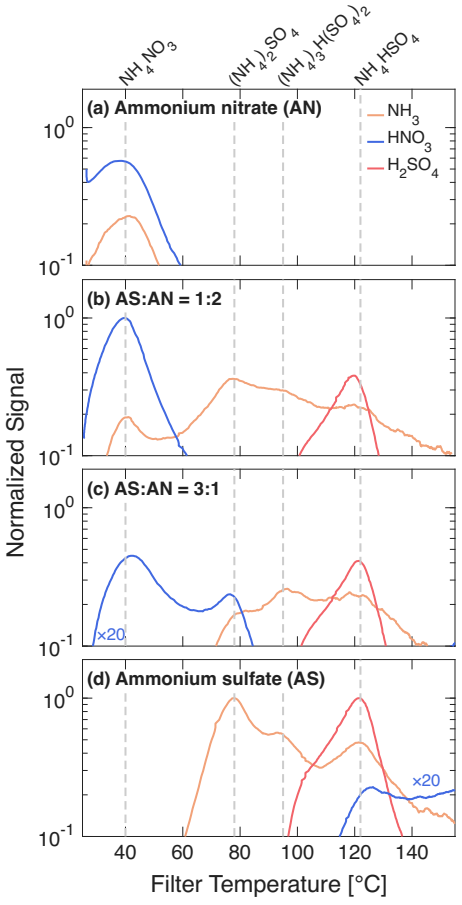

Figure 8. Thermograms of mixed ammonium nitrate and ammonium sulfate particles Thermograms of sulfuric acid (red), nitric acid (blue), and ammonia (orange) for atomized aqueous solutions of **(a)** pure ammonium nitrate, **(b)** ammonium sulfate-to-ammonium nitrate (AS:AN) = 1:2, **(c)** AS:AN = 3:1, and **(d)** pure ammonium sulfate. The nitric acid signal is multiplied by 20 in **(c)** and **(d)**, in the latter case showing nitrate contamination in the pure ammonium sulfate sample. Dashed vertical lines indicate the desorption temperatures associated with ammonium nitrate (NH_4NO_3), ammonium sulfate ($(NH_4)_2SO_4$), letovicite ($(NH_4)_3H(SO_4)_2$), and ammonium hydrogen sulfate (NH_4HSO_4) decomposition.

445 reaction. However, the ammonia thermogram retains three modes at the same temperatures as pure ammonium sulfate but with different relative intensities. This is consistent with nitric acid interacting with the ammonium sulfate lattice arrangement at higher sulfate concentrations.

4.4.2 Ambient aerosol

Lastly, we investigate ambient aerosol collected during the NYC-METS 2023 ground site campaign and analyzed at Aerodyne
450 Research Inc. (Billerica, MA) using the FIGAERO-BTOF. Figures 9a-b describe the filter collection site at the City University

https://doi.org/10.5194/egusphere-2026-4542
Preprint. Discussion started: 16 September 2026

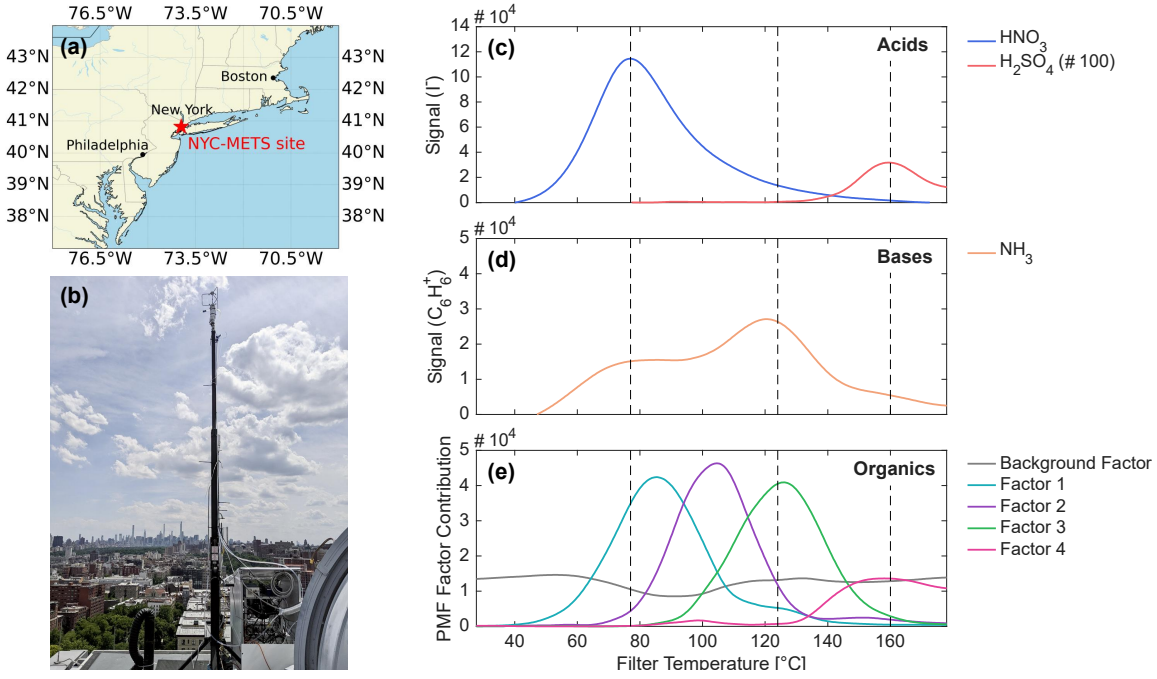

Figure 9. Acids, bases and organics measured in ambient aerosol. **(a)** Map of the NYC-METS filter collection site in New York, New York (40.82° N, 73.95° W), **(b)** a photograph of the site, **(c)** nitric acid (blue) and sulfuric acid (red) thermograms measured in the negative I^- mode (the sulfuric acid signal is multiplied by 100), **(d)** particulate ammonia (orange) measured by positive $C_6H_6^+$ chemical ionization, and **(e)** organic factors measured by negative I^- chemical ionization and grouped using positive matrix factorization (PMF). For the PMF analysis, five factors, including a background factor (grey), are used to explain the total signal. The factors exclude signal from the reagent ions (I^-, H_2OI^-), inorganic acids (HNO_3I^-, $H_2SO_4I^-$), and high background/contamination signals ($CH_2IO_2^-$, $C_3H_6IO_3^-$, $C_2F_3HIO_2^-$, $C_3F_5HIO_2^-$). The vertical dashed lines guide the eye between modes with similar desorption profiles. The base map was produced using Cartopy Natural Earth (Elson et al., 2024).

of New York (40.82° N, 73.95° W, 89 m above sea level). The average signal from two thermal desorption cycles of different sections of the same filter are shown in Figs. 9c-e, with the shaded region representing ±1 standard deviation. The negative I^- mode measured inorganic acids (Fig. 9c) and oxygenated organic molecules (Fig. 9e). Positive matrix factorization of the FIGAERO thermograms (Buchholz et al., 2020) produced four organic factors (labeled 1-4) and a background factor. Factors 1-4 shared similar average chemical compositions but distinct thermal desorption behavior. The average chemical composition for each factor was 1) $C_{4.8}H_{7.4}O_{4.5}N_{0.5}$, 2) $C_{4.8}H_{7.7}O_{4.5}N_{0.5}$, 3) $C_{4.1}H_{7.3}O_{4.2}N_{0.3}$, 4) $C_{4.6}H_{7.4}O_{4.8}N_{0.5}$. Ammonia was measured in the positive $C_6H_6^+$ channel (Fig. 9d).

Although nitric acid and sulfuric acid are both observed in the ambient sample, their desorption temperatures differ from laboratory mixtures of ammonium nitrate and ammonium sulfate (Fig. 8). Nitric acid dominates the ambient particles, with a much smaller fraction of sulfuric acid, which is displayed with a multiplication factor of 100. Nitric acid and ammonia desorb

https://doi.org/10.5194/egusphere-2026-4542
Preprint. Discussion started: 16 September 2026

together, consistent with ammonium nitrate decomposition though variations in $T_{\max}$ arise from different instrumental setups. There is a second mode in the ammonia trace appearing around 125 °C, without a coincident inorganic acid desorption. This ammonia mode corresponds well with PMF Factor 3 (green) which has an average chemical composition of $C_{4.8}H_{7.4}O_{4.5}N_{0.5}$. It also coincides with desorption of $C_2H_4O_3$ (e.g. glycolic acid), indicating that the ammonia may be bound with organic acids rather than sulfuric acid. Recent size-resolved TD-CIMS measurements of α-pinene oxidation products have identified a similar high temperature, low molecular weight factor with intensity-weighted composition of $C_{5.37}H_{6.34}O_{2.34}$, notably including $C_2HO_3^-$, $C_3H_3O_2^-$, and $C_3H_5O^-$ (Wakeen et al., 2026). These small ions were attributed to thermal decomposition due to their high inferred volatility and thus expected low particle fraction. However, the FIGAERO-BTOF measurements offer an alternative explanation requiring H transfer in the particle phase (acid-base stabilization), which can be identified by dual measurements of organic and ammonia counter ions.

In the ambient aerosol sample, sulfuric acid desorbs at a high temperature ($\sim$ 160 °C) suggesting it is neutralized; however, we do not observe a well-resolved, conincident ammonia signal. In addition to ammonia, organic Factor 4 desorbs in a similar temperature range as sulfuric acid and with a slightly more oxygenated chemical composition of $C_{4.6}H_{7.4}O_{4.8}N_{0.5}$, suggesting interactions between the species. Depending on aerosol chemical composition and phase state, oxygenated organics or other species may act as the proton donor to neutralize sulfuric acid.

Positive and negative ion chemistries are especially informative when unique modes in the thermograms can be resolved and correlated. Interpretations of the NH_3 thermograms in Fig. 9d are complicated by the potential for complex behavior as seen for AS and AN mixtures as well as the potential for organic salt formation. Moreover, since these measurements were performed on collected filters, they could also be subject to sampling artifacts, including reactive uptake of ammonia vapor during collection. Potential sampling artifacts can be reduced in the future with online FIGAERO-BTOF measurements. Multivariate analysis of the resulting positive and negative reagent ion thermograms as a function time could also further enable better identification of correlating features in the different species thermograms.

5 Conclusions

By coupling FIGAERO thermal desorption with rapid-switching bipolar time-of-flight mass spectrometry, we have explored the classic Langmuir-Hinshelwood problem of separating reactive and non-reactive condensation products. For samples with known thermodynamic properties, we can predict the driving force for condensation by comparing the rates of desorption versus reaction. In ambient aerosol, there are many weakly acidic, oxygenated organic molecules for which we lack standards and cannot easily predict if reactive or non-reactive pathways are favored. The simultaneous release of acids and bases, elucidated using the FIGAERO-BTOF, is a key feature of reactive uptake. For ammonium sulfate, the thermograms of atomized aerosol share characteristic features with those from chamber and ambient aerosol, supporting this method and extending the atomized aerosol thermograms to real-world cases. However, future work should focus on the complexities of ambient sampling, including potential confounding reactions occurring on the filter during sampling.

https://doi.org/10.5194/egusphere-2026-4542
Preprint. Discussion started: 16 September 2026

The desorption temperature of acids and bases is influenced by both the enthalpy of reaction and the organization of the condensed state. We have presented two examples where entropy matters: the lattice energy for inorganic acid-base systems and amphiphilic assembly of alkyl organosulfate surfactants. There remain open questions about how aerosol phase state and crystallinity affects surface reactions and subsequent desorption. Particle viscosity has been shown to affect thermal desorption of dioctyl sebacate (DOS) coated with alkane oxidation products; where smaller, more functionalized alkanes (C_{8-13}) increased the DOS desorption temperature compared to larger, less functionalized alkanes (C_{13-17}) (Galeazzo et al., 2024). However, another study on alkenes shows the opposite relationship between chain length and viscosity; attributed to increased intramolecular sterics in smaller molecules (Longnecker et al., 2025). Aerosol liquid water content will also likely influence the results but is not currently constrained in this study. All of the thermal desorption experiments were run with dry, heated nitrogen that may promote dehydration reactions and evaporation of acids through loss of water. While strong acids like H_2SO_4 are relatively resistant to evaporation down to 1.5% relative humidity at 15 °C (Stolzenburg et al., 2020), weaker acids like methanesulfonic acid are prone to evaporation at higher relative humidity, especially from acidic aerosol (Mauldin et al., 1999; Miljevic et al., 2025; Yu et al., 2026). This effect to be less important for atomized and dried particles and more important for droplets and deliquesced aerosol. Future work should investigate how ion mobility in samples with higher aerosol liquid water content affects multivalent ionic interactions.

Thermal desorption of atmospheric particles using the FIGAERO-BTOF can deepen our understanding of how they initially grew. The simple example is ammonia and nitric acid which co-condense via reactive uptake and likewise decompose together. The ammonium sulfate thermogram with three ammonia modes associated with decomposition reactions provides a new way to explore the relative strength of different ion interactions between the same acid and base molecules. The high desorption temperature of ammonium hydrogen sulfate is consistent with molecular measurements of sulfuric acid-ammonia nucleation. Nucleation and early growth is driven by ammonium hydrogen sulfate (as opposed to ammonium sulfate) because the effective vapor pressure of the second ammonia molecule is much higher than the first one, especially considering the Kelvin effect for the smallest particles and clusters. For gas-phase ratios of NH_3/H_2SO_4 ranging from 10 to 500, both negative and positive clusters grow from the sulfuric acid tetramer adding between 1 to 1.4 ammonia molecule for each additional sulfuric acid molecule (Schobesberger et al., 2015). Equimolar sulfuric acid and ammonia addition is consistent with growth by ammonium hydrogen sulfate whereas the upper range, which has 1.4 NH_3 for every sulfuric acid molecule, is consistent with the formation of stable letovicite crystal, and not ammonium sulfate.

For mixtures of ammonium sulfate and ammonium nitrate, nitric acid desorption appears bimodal and at higher temperatures associated with the decomposition of ammonium sulfate. Ice nucleation measurements show that very low sulfate to nitrate ratios of 10^{-4} can trigger crystallization of ammonium nitrate and ratios of 0.017 create particles with similar ice nucleating properties to desert dust (Ullrich et al., 2017; Wang et al., 2022). Thus, the results from standard salt solution cannot be extrapolated by just knowing the acids and bases present, but work on more complex systems is needed to interpret how different ionic species interact with each other. The ambient sample from the NYC-METS site demonstrates that the technique can be applied to more diverse aerosol but the positive and negative ionization chemistries are necessary to understand all

https://doi.org/10.5194/egusphere-2026-4542
Preprint. Discussion started: 16 September 2026

potential interactions. With this added complexity, tools tools like positive matrix factorization can identify key species that co-desorb and isolate surface reactions driving desorption.

Beyond inorganic acids, the FIGAERO-BTOF reveals new reasons why some organics exhibit suppressed volatility in the particle phase. For example, matrix effects have been show to decrease the apparent volatility of levoglucosan by up to four orders of magnitude (Xie et al., 2026). Multifunctional carboxylic acids can form a stable electrostatic network of hydrogen bonds in particles as small as 3 nm (Zhang et al., 2026). And, FIGAERO CIMS measurements frequently identify a large class of low molecular weight organics compounds in organic aerosol that are desorbing at higher temperatures (i.e. lower volatility) than predicted based on their chemical composition (Lopez-Hilfiker et al., 2016). The latter case is still widely regarded to be an artifact of thermal decomposition. These compounds have elemental compositions consistent with phthalic acid and pinonaldehyde (Zhao et al., 2013), pinic, pinonic, and norpinic acids (Lopez-Hilfiker et al., 2015; Lutz et al., 2019), isoprene epoxydiols (IEPOX) and IEPOX-derived methyltetrols (Lopez-Hilfiker et al., 2016), and glyoxylic acid (Schobesberger et al., 2018). Many of these compounds can carry either a negative charge (e.g. dicarboxylic acids) or a positive one (e.g. IEPOX), suggesting more complex electrostatic interactions are required to explain their behavior. For ionic species, we find that the Gibbs free energy of the neutralization reaction relates to desorption temperature more consistently than vapor pressure. Differentiating these species from decomposition products is important for understanding the overall acid content in particulate matter, as well as reallocating oligomeric mass. Particle composition measurements using the FIGAERO-BTOF can distinguish between reactive and non-reactive condensation products to assess what role organic reactive uptake plays in early particle growth. The atmospheric abundance of ionic organic compounds is important because they are non-volatile and stable while out of equilibrium with the gas phase. Thus lightweight organics, bound with inorganic acids and bases, can be transported across tropospheric regions and temperature largely resisting evaporation and promoting particle survival.

https://doi.org/10.5194/egusphere-2026-4542
Preprint. Discussion started: 16 September 2026

Appendix A

A1 Mass Spectrometers

Data in Figs. 1 and 2 were collected using a low pressure (150 mbar), turbulent ion molecular reactor (IMR) with unipolar chemical ionization time-flight-mass spectrometer, as previously operated with the FIGAERO inlet (Lopez-Hilfiker et al., 2014). The remaining figures used data from the Vocus B series (bipolar time-of-flight mass spectrometer) with resolution = 5000 (B2) or 10,000 (B4). The B4 instrument had deuterated organic reagents (i.e. $\mathrm{C_3D_6O}$ and $\mathrm{C_6D_6}$) and dibromomethane ($\mathrm{CH_2Br_2}$) was added to the acetone permeation tube. This produced the following reagent ion modes – bromide ($\mathrm{Br^-}$), deuterated acetone ($\mathrm{C_3D_6O^+}$), iodide ($\mathrm{I^-}$), and deuterated benzene ($\mathrm{C_6D_6^+}$). The Vocus B series use an adduct ionization mechanism (AIM) reactor (Riva et al., 2024) with pressure control maintained at 50 mbar for all experiments.

Table A1. Instrumental components for data presented in the main figures. The reagent ions for the negative and positive mode, if applicable, are listed and the scheme in **bold** was used for the data presented each figure.

		Front-end		**Detector**
	IMR	Negative polarity	Positive polarity	ToF
Fig. 1	turbulent	$\mathbf{I^-}$	n/a	unipolar
Fig. 2	turbulent	$\mathbf{I^-}$	n/a	unipolar
Fig. 3	AIM	$\mathrm{O_2^-}$, $\mathbf{I^-}$	$\mathbf{C_3H_6O^+}$, $\mathrm{C_6H_6^+}$	B2
Fig. 5	AIM	$\mathrm{Br^-}$, $\mathbf{I^-}$	$\mathrm{C_3D_6O^+}$, $\mathbf{C_6H_6^+}$	B4
Fig. 6	AIM	$\mathrm{O_2^-}$, $\mathbf{I^-}$	$\mathbf{C_3H_6O^+}$, C6H6+	B2
Fig. 7	AIM	$\mathrm{O_2^-}$, $\mathbf{I^-}$	$\mathbf{C_3H_6O^+}$, $\mathrm{C_6H_6^+}$	B2
Fig. 8	AIM	$\mathrm{O_2^-}$, $\mathbf{I^-}$	$\mathbf{C_3H_6O^+}$, $\mathrm{C_6H_6^+}$	B2
Fig. 9	AIM	$\mathrm{O_2^-}$, $\mathbf{I^-}$	$\mathbf{C_3H_6O^+}$, $\mathrm{C_6H_6^+}$	B2

A2 CLOUD chamber ammonium sulfate aerosol

Figure A1 compares aerosol produced from atomized $\mathrm{(NH_4)_2SO_4}$ solution (further referred to as atomized aerosol) and secondary aerosol produced from the condensation of sulfuric acid and ammonia vapors (i.e. chamber aerosol). The sulfuric acid thermograms are similar between the (a) atomized and (b) chamber aerosol, though the evaporation temperature (analogous to elapsed time) varies due to different heating rates. In Fig. A1e, the relative amplitudes of the ammonia modes for the chamber sample appear to be more equal compared to the atomized sample. Particularly, the ammonium sulfate decomposition (first) mode appears to have similar amplitude to the ammonium hydrogen sulfate (third) mode, suggesting the aerosol is not fully neutralized. The third column normalizes the integrated area of each $\mathrm{NH_3}$ mode by the total integrated $\mathrm{H_2SO_4}$ signal for each sample. Once the baseline is removed, the samples more closely resemble one another, though for the chamber sample, the ammonium sulfate (first) mode still appears lower than the ammonium hydrogen sulfate (third) mode, and the letovicite (sec-

https://doi.org/10.5194/egusphere-2026-4542
Preprint. Discussion started: 16 September 2026

ond) mode is less pronounced. The vapor pressure of ammonia is lowest when sulfuric acid is in excess so we expect efficient ammonia uptake, but nevertheless there may be insufficient ammonia to completely neutralize the particles to ammonium sulfate. In general, Fig. A1 demonstrates that the results from aerosol atomization can be extended to samples formed via reactive uptake in the atmosphere.

A3 PEG calibration

Temperature-programmed desorption follows a Langmuir adsorption isotherm where the rate of adsorption depends on temperature, pressure, and chemical composition. For FIGAERO CIMS, the rate of non-dissociative thermal desorption of aerosol particles is described by the Hertz-Knudsen equation (Hertz, 1882; Cappa et al., 2007; Schobesberger et al., 2018).

$$\frac{\mathrm{d}N_i}{\mathrm{d}t} = -\frac{1}{\sqrt{2\pi\, k_\mathrm{B}\, m_i\, T}} \cdot P_i^*(T) \cdot \chi_i \cdot \alpha \cdot \Gamma(\mathrm{Kn}) \cdot \mathrm{SA} \tag{A1}$$

where for compound i, N_i is the number of molecules in the particle phase, k_B is the Boltzmann constant, m_i is the molar mass of a molecule of i, T is temperature, P_i^* is the saturation vapor pressure, χ_i is a correction factor related to Raoult's law, α is the evaporation coefficient, Γ is a correction factor for gas diffusion, and SA is the particle surface area which governs the rate of gas-to-particle mass transfer (Schobesberger et al., 2018).

Polyethylene glycol (PEG) polymers with literature vapor pressures are used to calibrate a T_max-$\log c^*$ relationship for FIGAERO CIMS (Bannan et al., 2019; Ylisirniö et al., 2021, 2025). Typically, an aqueous mixture of PEG is atomized and collected on the filter and the aerosol is heated using the standard temperature ramp. A calibration curve is generated using a linear fit of the experimental T_max values to literature vapor pressure, P_sat (Krieger et al., 2018; Ylisirniö et al., 2021). Saturation vapor pressure is converted to volatility using Eq. A2.

$$C^*\left(\mu g \cdot m^{-3}\right) = \frac{P_\mathrm{sat} M_w}{RT} \times 10^6 \tag{A2}$$

where C^* is the saturation concentration, M_w is the molecular weight ($\mathrm{g\,mol^{-1}}$), R is the ideal gas constant (8.314 $\mathrm{J\,mol^{-1}\,K^{-1}}$), and T is temperature (K).

Table A2 summarizes the results of three independent calibrations for different instruments: Unipolar, B2, and B4 FIGAERO CIMS. All T_max values are obtained from thermograms using $\mathrm{I^-}$ reagent to detect PEG molecules. The calibration for the unipolar FIGAERO CIMS was performed at the CLOUD17 campaign occurring between Sep-Dec 2024. A 0.5 $\mathrm{g\,L^{-1}}$ solution of PEG-400 and deionized water was atomized to create aerosols which were subsequently passed through an aerosol dryer and collected on the filter at a rate of 1 $\mathrm{L\,min^{-1}}$. The filter mass loading was varied by adjusting the particle collection time to be 15, 20, 45, 60, 90, and 120 seconds. Table A2 shows the mean ($\mathrm{n} = 6$) for different mass loadings with the standard deviation less than or equal to ± 3.2 °C. The B2 instrument was calibrated at Aerodyne Research Inc. (Billerica, MA) in January 2025. The B4 instrument was calibrated at the CLOUD18 campaign (Geneva, Switzerland) in October 2025. Both B-series calibrations used a differential mobility analyzer (DMA) to select particle size and a condensation particle counter

https://doi.org/10.5194/egusphere-2026-4542
Preprint. Discussion started: 16 September 2026

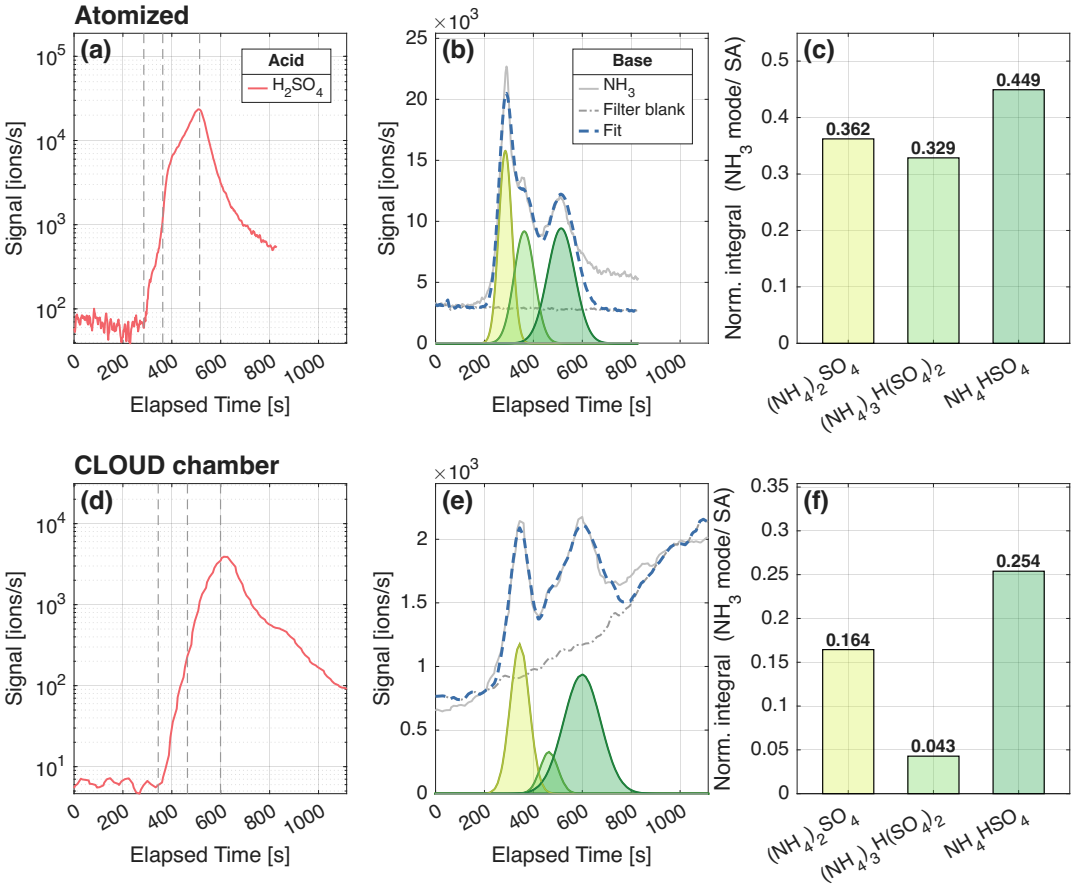

Figure A1. Comparison of ammonium sulfate thermograms for atomized versus CLOUD chamber aerosol. The two rows represent thermograms from atomized $(NH_4)_2SO_4$ solution and *in situ* aerosol formation in the CLOUD chamber, respectively. Thermograms are plotted against elapsed time of the temperature ramp used for peak integration and which is analogous to increasing temperature. The absolute difference in desorption time (i.e. temperature) between the two samples can be attributed to different instruments used and different heating rates. **(a, d)** Sulfuric acid thermograms are plotted in red in the first column with grey dashed lines marking the peak centers from the Gaussian curves used to fit the ammonia signal. The thermogram from atomized aerosol has a more pronounced shoulder around the second vertical line which is associated with letovicite decomposition. Sulfuric acid begins desorbing at the first ammonia mode (vertical line) with increasing signal until reaching a maximum at the third ammonia mode. **(b, e)** The total ammonia (NH_3) signal is plotted as a solid grey line in the second column, with the baseline plotted in dashed grey lines. Three Gaussian peaks with increasingly dark green color represent the decomposition of ammonium sulfate ($(NH_4)_2SO_4$), letovicite ($(NH_4)_3H(SO_4)_2$), and ammonium hydrogen sulfate (NH_4HSO_4), respectively. The total fit combined from the three Gaussian curves and the baseline is displayed in blue on top of the original ammonia trace. While this method generally fits the data well, we note that uniform Gaussian may not best explain the underlying chemical and physical processes. **(c, f)** The third column plots the integrated area ammonia modes where the height of each bar represents the ratio of the integrated ammonia mode divided by the total integrated sulfuric acid thermogram for each sample.

https://doi.org/10.5194/egusphere-2026-4542
Preprint. Discussion started: 16 September 2026

(CPC) to quantify particle number concentration and calculate filter mass loading. The B2 calibration used 0.5 $\mathrm{g\,L^{-1}}$ solution of PEG-600/HPLC water and the B4 calibration used a solution of 1 $\mathrm{g\,L^{-1}}$ PEG-400/Milli-Q water.

Calibration is important to account for variations between instrument configuration (e.g. thermocouple placement relative to the filter) and operation (e.g. rate of temperature ramp). Other factors affect the calibration beyond innate properties (i.e vapor pressure) and instrumental differences. Atomization, for example, produces results more consistent with ambient aerosol compared to syringe deposit of solution onto the filter (Ylisirniö et al., 2021). The particle physical properties also matter, notably particle diameter and overall mass loading on the filter. A previous study found small shifts ($\sim 7\ ^\circ\mathrm{C}$) in $T_{\max}$ varying with particle mobility diameter between 80 and 300 nm (i.e. surface area in the Hertz-Knudsen equation) (Cappa et al., 2007; Ylisirniö et al., 2021). However, our inter-comparison finds an even larger discrepancy where $T_{\max}$ can vary by over 20 $^\circ\mathrm{C}$ within a more narrow particle size range. Figure A2 shows the calibration curves for PEG particle size-selected to 40, 100, and 200 nm. While the slope of the calibration curve is relatively the same across the calibrations, the y-intercept decreases with particle surface area. For the comparison between atomized and chamber ammonium sulfate (Fig. A1), we observed the same relatively ordering of modes but the atomized sample modes appearing at higher temperatures. The atomized samples were size selected to 100 nm for which we have a calibration with the B2 instrument and multiple calibrations with the B4 instrument that occurred over multiple days. Ambient and chamber aerosol should use monodisperse calibrations corresponding to the size mode that will contribute most to overall surface area on the filter. Here, the calibration curve for the 40 nm PEG particles can be used when measuring smaller particles, but more detailed calibrations may be necessary to increase the accuracy of $\log c^*$. For the purposes of this study, observing reactive species that lack a $T_{\max}$-$\log c^*$ relationship, the presented calibrations are included primarily for reference for users that have different instruments.

https://doi.org/10.5194/egusphere-2026-4542
Preprint. Discussion started: 16 September 2026

Table A2. Summary of PEG calibrations

			T_{max} (°C)							
	D_p (nm)	~ µg	PEG-5	PEG-6	PEG-7	PEG-8	PEG-9	PEG-10	PEG-11	$\ln P_{sat} = m(T_{max}) + b$
Unipolar	n/a		-	50.2 ±3.2	70.9 ±3.0	88.9 ±2.4	106.1 ±1.4	124.9 ±3.0	144.2 ±2.0	$m = -0.161$ $b = -2.139$
B2	100	0.1	-	-	61.8	71.5	89.7	101.1	110.8	$m = -0.20$ $b = -1.25$
	200	2	43.2	58.4	75.2	92.2	106.7	118.7	131.3	$m = -0.18$ $b = 0.33$
B4	100	0.1	-	46.1	67.8	84.7	98.7	109.8	122.1	$m = -0.15$ $b = -3.45$
		0.1	-	46.2	67.6	83.9	97.2	118.3	126.8	$m = -0.17$ $b = -2.22$
		0.1	-	44.3	65.4	82.1	98.0	109.8	120.4	$m = -0.17$ $b = -2.89$
		0.1	-	43.8	64.7	82.1	98.7	110.4	117.8	$m = -0.16$ $b = -3.18$
		0.1	-	44.2	66.8	85.1	98.1	110.9	118.0	$m = -0.16$ $b = -2.98$
		0.1	-	41.9	64.2	80.9	95.2	107.4	115.0	$m = -0.17$ $b = -3.20$
			-	**44.9** **±1.1**	**66.1** **±1.5**	**83.1** **±1.7**	**97.7** **±1.3**	**111.1** **±3.7**	**120.0** **±4.1**	$\mathbf{m = -0.17}$ $\mathbf{b = -2.67}$
	40	0.09	-	-	54.0	69.7	84.3	94.8	101.5	$m = -0.19$ $b = -3.12$
		0.09	-	-	54.4	69.9	82.3	96.4	107.2	$m = -0.21$ $b = -2.16$
		0.09	-	-	51.8	66.4	82.3	95.2	104.1	$m = -0.19$ $b = -3.65$
		0.09	-	-	54.1	69.3	85.4	97.3	105.0	$m = -0.19$ $b = -3.47$
			-	-	**53.6** **±1.2**	**68.8** **±1.6**	**83.6** **±1.5**	**95.9** **±1.1**	**104.5** **±2.4**	$\mathbf{m = -0.19}$ $\mathbf{b = -3.11}$

https://doi.org/10.5194/egusphere-2026-4542
Preprint. Discussion started: 16 September 2026

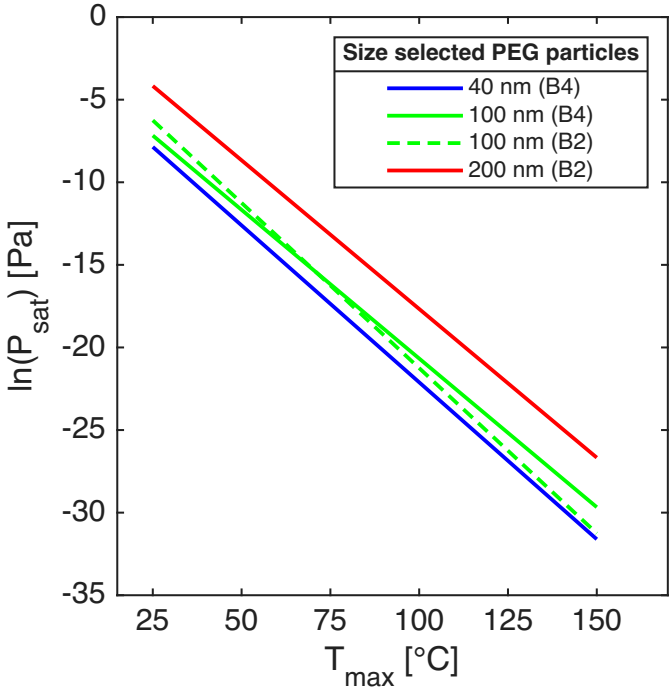

Figure A2. Calibration curves for monodisperse populations of 40 nm (blue), 100 nm (green), and 200 nm (red) PEG particles. For reference, the instrument used (B2 or B4) is shown in the legend. Variations in solution preparation, calibration set-up, heating ramp, and the unique FIGAERO inlets are likely to influence the calibration more than the base mass spectrometer.

A4 Thermogram slope-fitting

In the previous section (appendix A3), the saturation vapor pressure (P_{sat}) was experimentally determined using the temperature of maximum desorption (T_{max}) (Bannan et al., 2019). Similarly, the enthalpy of vaporization (ΔH) may be constrained by the thermogram upslope, where more shallow upslopes correspond to lower ΔH (Schobesberger et al., 2018). The upslope is obtained by a linear fit of the logarithmic thermogram signal ($\ln(I_{\mathrm{T}} - I_{\mathrm{T_0}})$) plotted as a function of inverse temperature ($1/T$), as an approximation of the Clausius Clapeyron equation (West et al., 2023).

$$\ln(p_T^*) \sim \ln(I_T - I_{\mathrm{T_0}}) = -\frac{\Delta H_{\mathrm{vap}}^*}{RT} + \mathrm{c} \tag{A3}$$

Though typically associated with the enthalpy of vaporization, the upslope can more broadly be considered the energy limiting the rate of evaporation. Figures A3 and A4 compare ΔH derived from the thermogram upslopes for the salts in this study, with polyethylene glycol (PEG) acting as a calibrant for classical evaporation driven solely by vapor pressure. The organic acids and organosulfates are plotted separately because they were measured using different instruments and consequently have different PEG references.

https://doi.org/10.5194/egusphere-2026-4542
Preprint. Discussion started: 16 September 2026

Figure A3 compares the upslopes for ammonium nitrate (blue), ammonium sulfate (red), ammonium oxalate (purple), and ammonium citrate (green), along with a PEG calibration performed during the experiments (black squares). The enthalpies of vaporization estimated using the upslopes of the PEG thermograms are biased low by approximately 20-50 $\mathrm{kJ\,mol^{-1}}$, compared to more a comprehensive treatment using the Hertz-Knudsen equation (eq. A1), as shown in grey crosses from Ylisirniö et al. (2025). This discrepancy is likely due to methodological differences, with a simpler line-fitting approach used for this study. For the acids, solid and empty square markers correspond to signal associated with the iodide adduct and deprotonated form, respectively. The plus markers indicate the ammonia evaporation temperature associated with each salt. For ammonium nitrate and ammonium oxalate, the acid and base markers for a given salt are clustered together, indicating their vaporization energies are similar. One notable exception is ammonium citrate where citric acid remains on the filter in its neutral form and desorbs at a higher temperature than ammonia. Ammonium sulfate behaves similarly since its decomposition produces gaseous ammonia while keeping sulfuric acid in the particle phase in the bisulfate state. In general, the markers lying above and below the PEG calibrations indicate other processes are affecting desorption beyond classical evaporation, though there is also variability in ΔH_{vap} a function of volatility (C^*).

Figure A4 shows the enthalpy of vaporization for the organosulfur species including methyl sulfate (pink), hydroxymethanesulfonic acid (red), ethyl sulfate (purple), butyl sulfate (blue), octyl sulfate (yellow), and decyl sulfate (orange). With the exception of butyl and ethyl sulfate, the longer chained alkyl organosulfates have steep upslopes, again suggesting a process other than classical evaporation occurs. Therefore, it is unlikely the Hertz-Knudsen equation, where the rate of evaporation is a function of vapor pressure, can appropriately describe the acid and base thermograms. Instead, a temperature-dependent Arrhenius equation could replace enthalpy of vaporization with activation energy (E_A).

https://doi.org/10.5194/egusphere-2026-4542
Preprint. Discussion started: 16 September 2026

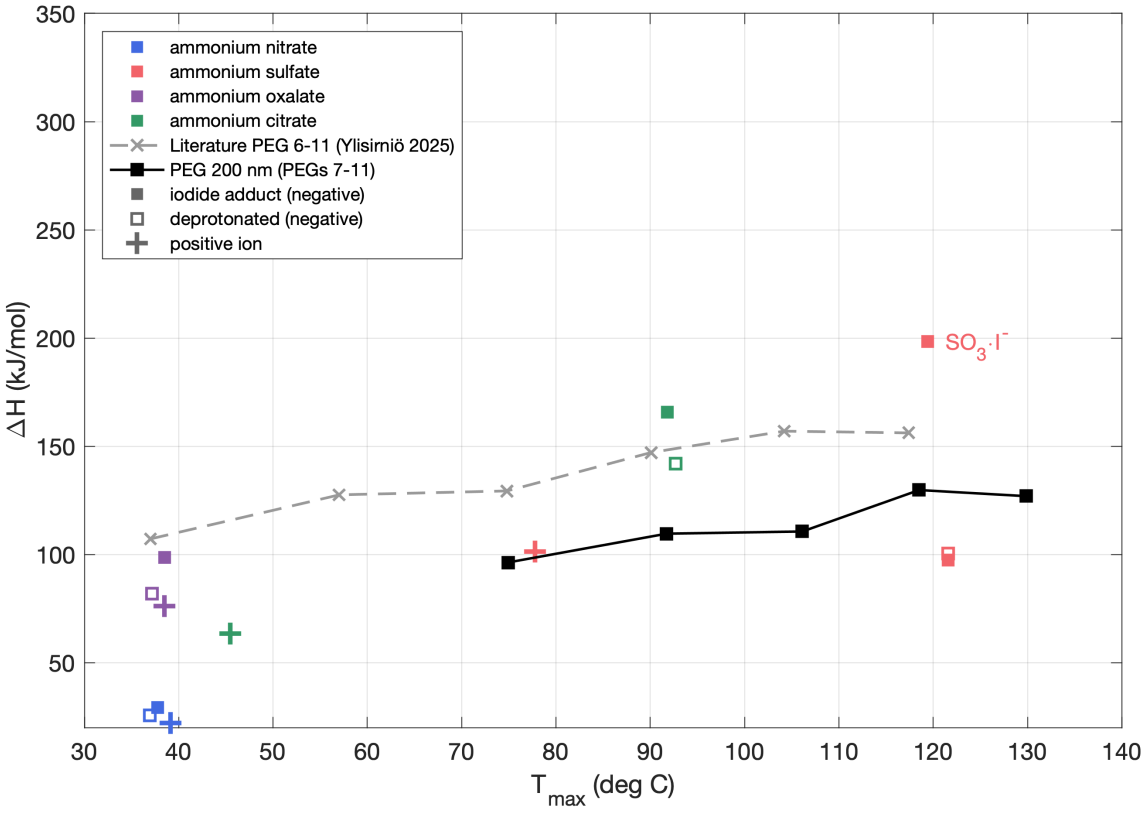

Figure A3. Enthalpy of vaporization derived by thermogram upslopes for inorganic and organic acids. Acids detected as an iodide adduct (filled square) and in the deprotonated form (empty square) are shown for ammonium nitrate (blue), ammonium sulfate (red), ammonium oxalate (purple), and ammonium citrate (green). Ammonia is shown in the corresponding color as a plus sign. The PEG calibration performed during these experiments is shown as black squares and the PEG calibration from Ylisirniö et al. (2025) is shown as grey crosses.

https://doi.org/10.5194/egusphere-2026-4542
Preprint. Discussion started: 16 September 2026

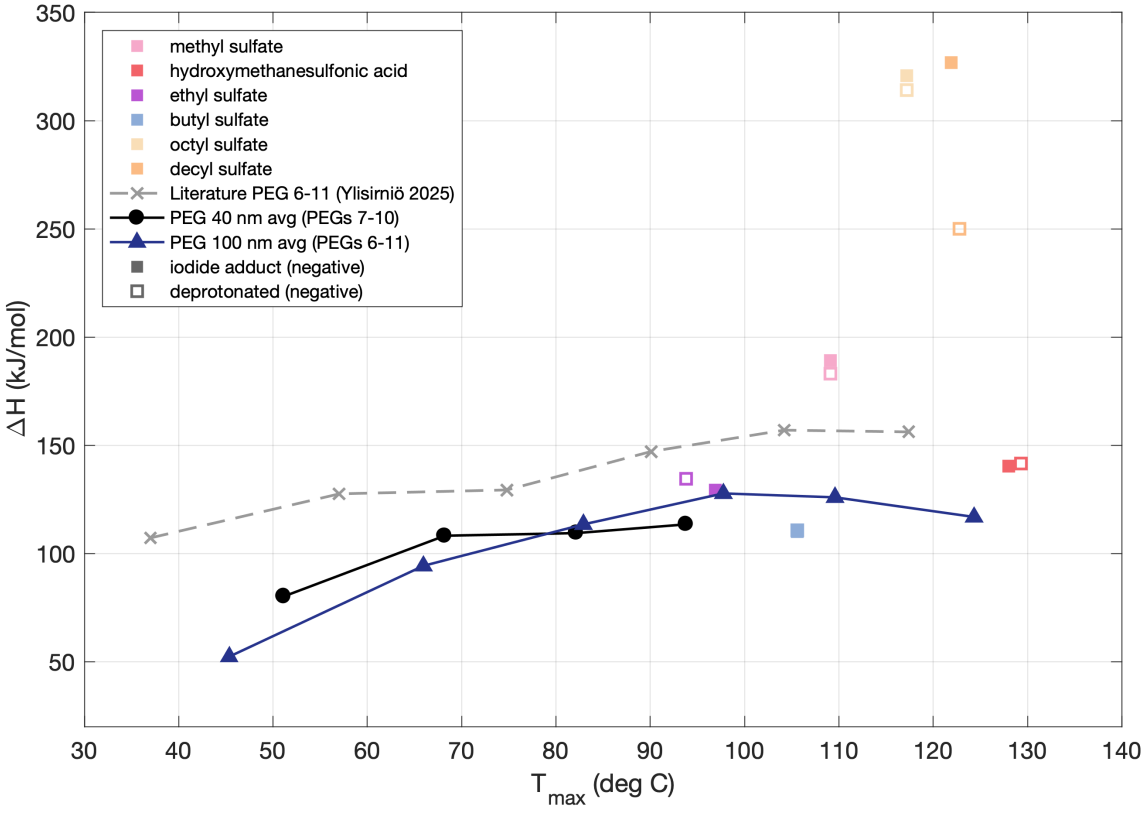

Figure A4. Enthalpy of vaporization derived by thermogram upslopes for organosulfur species. Acids detected as an iodide adduct (filled square) and in the deprotonated form (empty square) are shown for methyl sulfate (pink), hydroxymethanesulfonic acid (red), ethyl sulfate (purple), butyl sulfate (blue), octyl sulfate (yellow), and decyl sulfate (orange). Two calibrations were performed with the organosulfate experiments using size-selected PEG particles with diameters of 40 nm (black circles) and 100 nm (blue triangles). An independent PEG calibration using the Hertz-Knudsen equation to calculate H_{vap} is shown as grey crosses (Ylisirniö et al., 2025).

https://doi.org/10.5194/egusphere-2026-4542
Preprint. Discussion started: 16 September 2026

A5 Thermodynamics

Table A3. Reference thermodynamic values taken from, [a]CRC Handbook of Chemistry and Physics. *106th Edition* (**?**), [b]Scott & Cattell, 1979 (Scott and Cattell, 1979), [c]Gmitro & Vermuelen, 1963 (Gmitro and Vermuelen, 1963). **Bold values** are used to calculate reaction thermodynamics in Table A4.

	ΔH_f^{298K} (kJ mol^{-1})	S_f^{298K} (J mol^{-1} K^{-1})	ΔG_f^{298K} (kJ mol^{-1})	pK_{a1}	pK_{a2}
$NH_{3(g)}$	$\mathbf{-45.9}^a$	$\mathbf{192.8}^a$	-16.4^a	9.25	
$HNO_{3(g)}$	-133.9^a	266.9^a	-73.5^a	-1.5	
$HNO_{3(l)}$	$\mathbf{-174.1}^a$	$\mathbf{155.6}^a$	-80.7^a	-1.5	
$H_2SO_{4(g)}$	-732.2^c	156.9^c	-651.2^c	-3	1.92
$H_2SO_{4(l)}$	$\mathbf{-814.9}^a$	$\mathbf{156.9}^a$	-690.0^a	-3	1.92
$NH_4NO_{3(s)}$	$\mathbf{-365.6}^a$	$\mathbf{151.1}^a$	-183.9^a		
$(NH_4)HSO_{4(s)}$	$\mathbf{-1027.0}^a$	$\mathbf{150.6}^b$	-803.7^b		
$(NH_4)_2SO_{4(s)}$	-1180.9^a	220.1^a	-901.7^a		

Table A4. Reaction thermodynamics for ammonium sulfate and ammonium nitrate decomposition. The values for $(NH_4)_2SO_4$ decomposition to ammonium hydrogen sulfate, $(NH_4)HSO_4$ are taken from Scott & Cantell, 1979 (Scott and Cattell, 1979). The remaining values are calculated using the thermodynamic properties of the pure substances in Table A3. **Bold values** are used in the van 't Hoff plot in Fig. 4 of the main text.

	ΔH_{rxn}^{298K} (kJ mol^{-1})	ΔS_{rxn}^{298K} (J mol^{-1} K^{-1})	ΔG_{rxn}^{298K} (kJ mol^{-1})	$\ln(K_{eq}^{298K})$
$(NH_4)_2SO_{4(s)} \leftrightharpoons (NH_4)HSO_{4(s)} + NH_{3(g)}$	**124.6**	**123.0**	87.9	**-35.5**
$(NH_4)HSO_{4(s)} \leftrightharpoons H_2SO_{4(l)} + NH_{3(g)}$	**166.2**	**226.2**	97.3	**-39.8**
$H_2SO_{4(l)} \leftrightharpoons H_2SO_{4(g)}$	82.7		38.8	
Net: $(NH_4)_2SO_{4(s)} \leftrightharpoons H_2SO_{4(g)} + 2NH_{3(g)}$	356.9		217.7	
$NH_4NO_{3(s)} \leftrightharpoons HNO_{3(l)} + NH_{3(g)}$	**145.6**	**197.2**	86.8	**-35.0**
$HNO_{3(1)} \leftrightharpoons HNO_{3(g)}$	40.2		7.2	
Net: $NH_4NO_{3(s)} \leftrightharpoons HNO_{3(g)} + NH3_{3(g)}$	185.8		94.0	

https://doi.org/10.5194/egusphere-2026-4542
Preprint. Discussion started: 16 September 2026

Data availability. Data for all figures in the main text and appendices will be made available at the Zenodo repository 10.5281/zenodo.21686407.

Author contributions. The study was conceptualized by J.D., M.C., and N.M.D. The methodology was developed by J.D., A.S., M.A., F.L.H., M.C., and N.M.D. The data was curated and collected by J.D., A.S., M.A., M.W., L. Hao, and C.L. The ambient filters from NYC-METS were collected by M.R. and D.G. Resources were provided by M.A., F.L.H., D.W., and M.C. All authors contributed to the scientific discussion and interpretation of the results. The original draft was written by J.D. and edited by A.S., N.B., S.S., M.R., A.V., N.B., C.L., D.M.R., E.S., L. Heikkinen, R.V., J.K., M.C., and N.M.D.

Competing interests. At least one of the (co-)authors is a member of the editorial board of Atmospheric Chemistry and Physics.

Acknowledgements. The authors thank the entire CLOUD collaboration as well as CERN for supporting CLOUD with important technical and financial resources and for providing a particle beam from the CERN Proton Synchrotron. J.D. acknowledges support from by Scott Institute and the Steinbrenner Institute Doctoral Fellowship at Carnegie Mellon University. N.B. acknowledges funding from Federal Ministry of Education and Research (BMBF) financed project CLOUD-22 01LK2201A. S.S. acknowledges funding from the Academy of Finland (grant no. 364229) and the Visiting Fellowship Program of the Cooperative Institute for Research in Environmental Sciences. M.J.R. acknowledges support from the NSF Graduate Research Fellowship (2139841). C.L. AND R.V. acknowledge funding from the National Science Foundation (NSF-AGS-2215522 & 2528506). D.R.G. acknowledges funding from NOAA AC-4 (NA20OAR4310304). L. Heikkinen acknowledges support from the INTEGRATE project, funded by the European Research Council Consolidator Grant (no. 865799) and Knut och Alice Wallenbergs Stiftelse (grant nos. 2021.0169, 2021.0298, 2023.0347). N.M.D. acknowledges funding from the National Science Foundation (NSF-AGS-2431817 and AGS-2528505).

https://doi.org/10.5194/egusphere-2026-4542
Preprint. Discussion started: 16 September 2026

References

Ayers, G. P., Gillett, R. W., and Gras, J. L.: On the vapor pressure of sulfuric acid, Geophysical Research Letters, 7, 433–436, https://doi.org/10.1029/GL007i006p00433, 1980.

Baalbaki, R., Shen, J., Simon, M., Klebach, H., Ruhl, S., DeVivo, J., Wang, M., Scholz, W., Dada, L., Rörup, B., Stolzenburg, D., Manninen, H. E., Sommer, E., Caudillo-Plath, L., Marie, G., Friedrich, M., Yu, W., Leiminger, M., Alfaouri, D., Amorim, A., Arnoldi-Meadows, T., Beckmann, H., Berntheusel, M., Bräkling, S., Brasseur, Z., Chiu, R., Duplissy, J., Finkenzeller, H., Heinritzi, M., Kunkler, F., Lamkaddam, H., Lopez, B., Mahfouz, N., Makhmutov, V., Martinez, M., Marten, R., Massabo, D., Mauldin, R., Mentler, B., Müller, M., Philippov, M., Piedehierro, A. A., Rato, P., Reinecke, T., Richter, S., Russell, D. M., Schulze, B., Surdu, M., Thakur, R. C., Tham, Y. J., Tian, P., Tomé, A., Tong, Y., Top, J., Wagner, A. C., Wang, D. S., Wang, Y., Ward, R. X., Weber, S. K., Welti, A., Wu, Y., Zauner-Wieczorek, M., Zhang, J., Curtius, J., Donahue, N. M., El Haddad, I., Flagan, R. C., Hansel, A., Harder, H., Kürten, A., Petäjä, T., Schobesberger, S., Sipilä, M., Volkamer, R., Winkler, P. M., Worsnop, D. R., Christoudias, T., Pozzer, A., Kulmala, M., Kirkby, J., Lehtipalo, K., and He, X.-C.: Role of methanesulfonic acid in atmospheric particle nucleation and growth, Nature, https://doi.org/10.1038/s41586-026-10810-2, 2026.

Bannan, T. J., Le Breton, M., Priestley, M., Worrall, S. D., Bacak, A., Marsden, N. A., Mehra, A., Hammes, J., Hallquist, M., Alfarra, M. R., Krieger, U. K., Reid, J. P., Jayne, J., Robinson, W., McFiggans, G., Coe, H., Percival, C. J., and Topping, D.: A method for extracting calibrated volatility information from the FIGAERO-HR-ToF-CIMS and its experimental application, Atmospheric Measurement Techniques, 12, 1429–1439, https://doi.org/10.5194/amt-12-1429-2019, 2019.

Bernales, C.: Kirk-Othmer Encyclopedia of Chemical Technology, 1981.

Bhattacharyya, N., Lopez, B., DeVivo, J., Russell, D. M., Shen, J., Sommer, E., Almeida, J., Amorim, A., Beckmann, H. M., Busato, M., Canagaratna, M. R., Caudillo, L., Chassaing, A., Christoudias, T., Dada, L., El-Haddad, I., Flagan, R. C., Harder, H., Judmaier, B., Kaniyodical Sebastian, M., Kirkby, J., Klebach, H., Kulmala, M., Kunkler, F., Lehtipalo, K., Liu, L., Mentler, B., Möhler, O., Morawiec, A., Petäjä, T., Rato, P., Rörup, B., Ruhl, S., Scholz, W., Simon, M., Tóme, A., Tong, Y., Top, J., Umo, N. S., Volkamer, R., Weissbacher, J., Worsnop, D. R., Xenofontos, C., Yang, B., Yu, W., Zauner-Wieczorek, M., Zgheib, I., Zhang, J., Zheng, Z., He, X.-C., Stolzenburg, D., Schobesberger, S., Curtius, J., and Donahue, N. M.: Isoprene Aerosol Growth in the Upper Troposphere: Application of the Diagonal Volatility Basis Set to CLOUD Chamber Measurements, ACS ES&T Air, 2, 2092–2104, https://doi.org/10.1021/acsestair.5c00106, _eprint: https://doi.org/10.1021/acsestair.5c00106, 2025.

Bilde, M., Svenningsson, B., Mønster, J., and Rosenørn, T.: Even Odd Alternation of Evaporation Rates and Vapor Pressures of C3 through C9 Dicarboxylic Acid Aerosols, Environmental Science & Technology, 37, 1371–1378, https://doi.org/10.1021/es0201810, 2003.

Blando, J. D. and Turpin, B. J.: Secondary organic aerosol formation in cloud and fog droplets: a literature evaluation of plausibility, Atmospheric Environment, 34, 1623–1632, https://doi.org/10.1016/S1352-2310(99)00392-1, 2000.

Brüggemann, M., Xu, R., Tilgner, A., Kwong, K. C., Mutzel, A., Poon, H. Y., Otto, T., Schaefer, T., Poulain, L., Chan, M. N., and Herrmann, H.: Organosulfates in Ambient Aerosol: State of Knowledge and Future Research Directions on Formation, Abundance, Fate, and Importance, Environmental Science & Technology, 54, 3767–3782, https://doi.org/10.1021/acs.est.9b06751, 2020.

Brüggemann, M., Riva, M., Perrier, S., Poulain, L., George, C., and Herrmann, H.: Overestimation of Monoterpene Organosulfate Abundance in Aerosol Particles by Sampling in the Presence of SO_2, Environmental Science & Technology Letters, 8, 206–211, https://doi.org/10.1021/acs.estlett.0c00814, 2021.

https://doi.org/10.5194/egusphere-2026-4542
Preprint. Discussion started: 16 September 2026

Buchholz, A., Ylisirniö, A., Huang, W., Mohr, C., Canagaratna, M., Worsnop, D. R., Schobesberger, S., and Virtanen, A.: Deconvolution of FIGAERO–CIMS thermal desorption profiles using positive matrix factorisation to identify chemical and physical processes during particle evaporation, Atmospheric Chemistry and Physics, 20, 7693–7716, https://doi.org/10.5194/acp-20-7693-2020, 2020.

Cai, J., Daellenbach, K. R., Wu, C., Zheng, Y., Zheng, F., Du, W., Haslett, S. L., Chen, Q., Kulmala, M., and Mohr, C.: Characterization of offline analysis of particulate matter with FIGAERO-CIMS, Atmospheric Measurement Techniques, 16, 1147–1165, https://doi.org/10.5194/amt-16-1147-2023, 2023.

Cappa, C. D., Lovejoy, E. R., and Ravishankara, A. R.: Determination of Evaporation Rates and Vapor Pressures of Very Low Volatility Compounds: A Study of the C_4 -C_{10} and C_{12} Dicarboxylic Acids, The Journal of Physical Chemistry A, 111, 3099–3109, https://doi.org/10.1021/jp068686q, 2007.

Chebbi, A. and Carlier, P.: Carboxylic acids in the troposphere, occurrence, sources, and sinks: A review, Atmospheric Environment, 30, 4233–4249, https://doi.org/10.1016/1352-2310(96)00102-1, 1996.

Compernolle, S., Ceulemans, K., and Müller, J.-F.: EVAPORATION: a new vapour pressure estimation methodfor organic molecules including non-additivity and intramolecular interactions, Atmospheric Chemistry and Physics, 11, 9431–9450, https://doi.org/10.5194/acp-11-9431-2011, 2011.

Crahan, K. K., Hegg, D., Covert, D. S., and Jonsson, H.: An exploration of aqueous oxalic acid production in the coastal marine atmosphere, Atmospheric Environment, 38, 3757–3764, https://doi.org/10.1016/j.atmosenv.2004.04.009, 2004.

D'Ambro, E. L., Schobesberger, S., Gaston, C. J., Lopez-Hilfiker, F. D., Lee, B. H., Liu, J., Zelenyuk, A., Bell, D., Cappa, C. D., Helgestad, T., Li, Z., Guenther, A., Wang, J., Wise, M., Caylor, R., Surratt, J. D., Riedel, T., Hyttinen, N., Salo, V.-T., Hasan, G., Kurtén, T., Shilling, J. E., and Thornton, J. A.: Chamber-based insights into the factors controlling epoxydiol (IEPOX) secondary organic aerosol (SOA) yield, composition, and volatility, Atmospheric Chemistry and Physics, 19, 11 253–11 265, https://doi.org/10.5194/acp-19-11253-2019, 2019.

Dean, J. A.: Handbook of Organic Chemistry, McGraw-Hill, New York, ISBN 978-0-07-016193-1, 1987.

Dixon, P.: Formation of Sulphamic Acid during the Thermal Decomposition of Ammonium Sulphate, Nature, 154, 706–706, https://doi.org/10.1038/154706a0, 1944.

Donahue, N. M., Robinson, A. L., Stanier, C. O., and Pandis, S. N.: Coupled Partitioning, Dilution, and Chemical Aging of Semivolatile Organics, Environmental Science & Technology, 40, 2635–2643, https://doi.org/10.1021/es052297c, 2006.

Donahue, N. M., Epstein, S. A., Pandis, S. N., and Robinson, A. L.: A two-dimensional volatility basis set: 1. organic-aerosol mixing thermodynamics, Atmospheric Chemistry and Physics, 11, 3303–3318, https://doi.org/10.5194/acp-11-3303-2011, 2011.

Donahue, N. M., Xiao, M., Marten, R., Wang, M., Kong, W., Schervish, M., Ye, Q., Hofbauer, V., Dada, L., Duplissy, J., Finkenzeller, H., Gordon, H., Kirkby, J., Lamkaddam, H., Makhmutov, V., Philippov, M., Rörup, B., Volkamer, R., Wang, D., Weber, S. K., Flagan, R. C., Stolzenburg, D., and El Hadad, I.: Low temperature growth of sub 10 nm particles by ammonium nitrate condensation, Environmental Science: Atmospheres, 5, 67–81, https://doi.org/10.1039/d4ea00117f, publisher: Royal Society of Chemistry (RSC), 2025.

Donahue, N. M., Dada, L., Stolzenburg, D., Sommer, E., Simon, M., Schervish, M., DeVivo, J., Stinchfield, A., Burton, N., Bhattacharyya, N., Lopez, B., Wang, M., Scholz, W., Almeida, J., Zhao, B., Heinritzi, M., Gordon, H., Hansel, A., Curtius, J., Lehtipalo, K., El Haddad, I., Kirkby, J., Flagan, R., Kulmala, M., and Worsnop, D.: On describing particle nucleation within the Volatility Basis Set, Atmospheric Chemistry and Physics, 26, 8311–8339, https://doi.org/10.5194/acp-26-8311-2026, 2026.

Dovrou, E., Lim, C. Y., Canagaratna, M. R., Kroll, J. H., Worsnop, D. R., and Keutsch, F. N.: Measurement techniques for identifying and quantifying hydroxymethanesulfonate (HMS) in an aqueous matrix and particulate matter using aerosol mass spectrometry and ion chromatography, Atmospheric Measurement Techniques, 12, 5303–5315, https://doi.org/10.5194/amt-12-5303-2019, 2019.

https://doi.org/10.5194/egusphere-2026-4542
Preprint. Discussion started: 16 September 2026

Drozd, G., Woo, J., Häkkinen, S. A. K., Nenes, A., and McNeill, V. F.: Inorganic salts interact with oxalic acid in submicron particles to form material with low hygroscopicity and volatility, Atmospheric Chemistry and Physics, 14, 5205–5215, https://doi.org/10.5194/acp-14-5205-2014, 2014.

Du, M., Voliotis, A., Shao, Y., Wang, Y., Bannan, T. J., Pereira, K. L., Hamilton, J. F., Percival, C. J., Alfarra, M. R., and McFiggans, G.: Combined application of online FIGAERO-CIMS and offline LC-Orbitrap mass spectrometry (MS) to characterize the chemical composition of secondary organic aerosol (SOA) in smog chamber studies, Atmospheric Measurement Techniques, 15, 4385–4406, https://doi.org/10.5194/amt-15-4385-2022, 2022.

Edwards, G. D. and Clayton, F. E.: Patty's Industrial Hygiene and Toxicology. Volume 2A, 2B, 2C: Toxicology., Wiley, New York, 3., rev. ed edn., ISBN 978-0-471-16042-7, num Pages: 1467, 1981.

Elson, P., de Andrade, E. S., Lucas, G., May, R., Hattersley, R., Campbell, E., Comer, R., Dawson, A., Little, B., Raynaud, S., scmc72, Snow, A. D., lgolston, Blay, B., Killick, P., lbdreyer, Peglar, P., Wilson, N., Andrew, Szymaniak, J., Berchet, A., Bosley, C., Davis, L., Filipe, Krasting, J., Bradbury, M., stephenworsley, and Kirkham, D.: SciTools/cartopy: REL: v0.24.1, https://doi.org/10.5281/ZENODO.1182735, 2024.

Epstein, S. A., Riipinen, I., and Donahue, N. M.: A Semiempirical Correlation between Enthalpy of Vaporization and Saturation Concentration for Organic Aerosol, Environmental Science & Technology, 44, 743–748, https://doi.org/10.1021/es902497z, 2010.

Erdey, L., Gál, S., and Liptay, G.: Thermoanalytical properties of analytical-grade reagents, Talanta, 11, 913–940, https://doi.org/10.1016/0039-9140(64)80128-4, publisher: Elsevier BV, 1964.

Galeazzo, T., Aumont, B., Camredon, M., Valorso, R., Lim, Y. B., Ziemann, P. J., and Shiraiwa, M.: Secondary organic aerosols derived from intermediate-volatility n-alkanes adopt low-viscous phase state, Atmospheric Chemistry and Physics, 24, 5549–5565, https://doi.org/10.5194/acp-24-5549-2024, 2024.

Gmitro, J. I. and Vermuelen, T.: Vapor-liquid equilbrium for aqueous sulfuric acid., UCRL-10886, Univ of California, Lawrence Radiation Lab, 1963.

Gordon, H., Kirkby, J., Baltensperger, U., Bianchi, F., Breitenlechner, M., Curtius, J., Dias, A., Dommen, J., Donahue, N. M., Dunne, E. M., Duplissy, J., Ehrhart, S., Flagan, R. C., Frege, C., Fuchs, C., Hansel, A., Hoyle, C. R., Kulmala, M., Kürten, A., Lehtipalo, K., Makhmutov, V., Molteni, U., Rissanen, M. P., Stozkhov, Y., Tröstl, J., Tsagkogeorgas, G., Wagner, R., Williamson, C., Wimmer, D., Winkler, P. M., Yan, C., and Carslaw, K. S.: Causes and importance of new particle formation in the present-day and preindustrial atmospheres, Journal of Geophysical Research: Atmospheres, 122, 8739–8760, https://doi.org/10.1002/2017JD026844, 2017.

Gramlich, Y., Spahr, R., Upadhyay, A., Siegel, K., Haslett, S. L., Krejci, R., Yttri, K. E., and Mohr, C.: A Machine Learning Approach to Understand Thermal Desorption Profiles of Levoglucosan from FIGAERO–CIMS, Environmental Science & Technology, 60, 15 101–15 112, https://doi.org/10.1021/acs.est.5c18488, 2026.

Halstead, W. D.: Thermal decomposition of ammonium sulphate, Journal of Applied Chemistry, 20, 129–132, https://doi.org/10.1002/jctb.5010200408, publisher: Wiley, 1970.

Hao, L., Romakkaniemi, S., Kortelainen, A., Jaatinen, A., Portin, H., Miettinen, P., Komppula, M., Leskinen, A., Virtanen, A., Smith, J. N., Sueper, D., Worsnop, D. R., Lehtinen, K. E. J., and Laaksonen, A.: Aerosol Chemical Composition in Cloud Events by High Resolution Time-of-Flight Aerosol Mass Spectrometry, Environmental Science & Technology, 47, 2645–2653, https://doi.org/10.1021/es302889w, 2013.

Hass-Mitchell, T., Joo, T., Rogers, M., Nault, B. A., Soong, C., Tran, M., Seo, M., Machesky, J. E., Canagaratna, M., Roscioli, J., Claflin, M. S., Lerner, B. M., Blomdahl, D. C., Misztal, P. K., Ng, N. L., Dillner, A. M., Bahreini, R., Russell, A., Krechmer, J. E., Lambe, A.,

https://doi.org/10.5194/egusphere-2026-4542
Preprint. Discussion started: 16 September 2026

and Gentner, D. R.: Increasing Contributions of Temperature-Dependent Oxygenated Organic Aerosol to Summertime Particulate Matter in New York City, ACS ES&T Air, 1, 113–128, https://doi.org/10.1021/acsestair.3c00037, 2024.

He, X.-C., Tham, Y. J., Dada, L., Wang, M., Finkenzeller, H., Stolzenburg, D., Iyer, S., Simon, M., Kürten, A., Shen, J., Rörup, B., Rissanen, M., Schobesberger, S., Baalbaki, R., Wang, D. S., Koenig, T. K., Jokinen, T., Sarnela, N., Beck, L. J., Almeida, J., Amanatidis, S., Amorim, A., Ataei, F., Baccarini, A., Bertozzi, B., Bianchi, F., Brilke, S., Caudillo, L., Chen, D., Chiu, R., Chu, B., Dias, A., Ding, A., Dommen, J., Duplissy, J., El Haddad, I., Gonzalez Carracedo, L., Granzin, M., Hansel, A., Heinritzi, M., Hofbauer, V., Junninen, H., Kangasluoma, J., Kemppainen, D., Kim, C., Kong, W., Krechmer, J. E., Kvashin, A., Laitinen, T., Lamkaddam, H., Lee, C. P., Lehtipalo, K., Leiminger, M., Li, Z., Makhmutov, V., Manninen, H. E., Marie, G., Marten, R., Mathot, S., Mauldin, R. L., Mentler, B., Möhler, O., Müller, T., Nie, W., Onnela, A., Petäjä, T., Pfeifer, J., Philippov, M., Ranjithkumar, A., Saiz-Lopez, A., Salma, I., Scholz, W., Schuchmann, S., Schulze, B., Steiner, G., Stozhkov, Y., Tauber, C., Tomé, A., Thakur, R. C., Väisänen, O., Vazquez-Pufleau, M., Wagner, A. C., Wang, Y., Weber, S. K., Winkler, P. M., Wu, Y., Xiao, M., Yan, C., Ye, Q., Ylisirniö, A., Zauner-Wieczorek, M., Zha, Q., Zhou, P., Flagan, R. C., Curtius, J., Baltensperger, U., Kulmala, M., Kerminen, V.-M., Kurtén, T., Donahue, N. M., Volkamer, R., Kirkby, J., Worsnop, D. R., and Sipilä, M.: Role of iodine oxoacids in atmospheric aerosol nucleation, Science, 371, 589–595, https://doi.org/10.1126/science.abe0298, 2021.

Hertz, H.: Ueber die Verdunstung der Flüssigkeiten, insbesondere des Quecksilbers, im luftleeren Raume, Annalen der Physik, 253, 177–193, https://doi.org/10.1002/andp.18822531002, 1882.

Hilal, S., Karickhoff, S., and Carreira, L.: Prediction of the Vapor Pressure Boiling Point, Heat of Vaporization and Diffusion Coefficient of Organic Compounds, QSAR & Combinatorial Science, 22, 565–574, https://doi.org/10.1002/qsar.200330812, 2003.

Hyttinen, N., Elm, J., Malila, J., Calderón, S. M., and Prisle, N. L.: Thermodynamic properties of isoprene- and monoterpene-derived organosulfates estimated with COSMO *therm*, Atmospheric Chemistry and Physics, 20, 5679–5696, https://doi.org/10.5194/acp-20-5679-2020, 2020.

Jayne, J. T., Leard, D. C., Zhang, X., Davidovits, P., Smith, K. A., Kolb, C. E., and Worsnop, D. R.: Development of an Aerosol Mass Spectrometer for Size and Composition Analysis of Submicron Particles, Aerosol Science and Technology, 33, 49–70, https://doi.org/10.1080/027868200410840, 2000.

Ji, Y., Huey, L. G., Tanner, D. J., Lee, Y. R., Veres, P. R., Neuman, J. A., Wang, Y., and Wang, X.: A vacuum ultraviolet ion source (VUV-IS) for iodide–chemical ionization mass spectrometry: a substitute for radioactive ion sources, Atmospheric Measurement Techniques, 13, 3683–3696, https://doi.org/10.5194/amt-13-3683-2020, 2020.

Kaniewski, M., Biegun, M., and Hoffmann, J.: Thermal stability of systems containing ammonium nitrate and sulfate salts: an experimental study, Journal of Thermal Analysis and Calorimetry, 148, 13 051–13 064, https://doi.org/10.1007/s10973-023-12328-5, publisher: Springer Science and Business Media LLC, 2023.

Kirkby, J., Curtius, J., Almeida, J., Dunne, E., Duplissy, J., Ehrhart, S., Franchin, A., Gagné, S., Ickes, L., Kürten, A., Kupc, A., Metzger, A., Riccobono, F., Rondo, L., Schobesberger, S., Tsagkogeorgas, G., Wimmer, D., Amorim, A., Bianchi, F., Breitenlechner, M., David, A., Dommen, J., Downard, A., Ehn, M., Flagan, R. C., Haider, S., Hansel, A., Hauser, D., Jud, W., Junninen, H., Kreissl, F., Kvashin, A., Laaksonen, A., Lehtipalo, K., Lima, J., Lovejoy, E. R., Makhmutov, V., Mathot, S., Mikkilä, J., Minginette, P., Mogo, S., Nieminen, T., Onnela, A., Pereira, P., Petäjä, T., Schnitzhofer, R., Seinfeld, J. H., Sipilä, M., Stozhkov, Y., Stratmann, F., Tomé, A., Vanhanen, J., Viisanen, Y., Vrtala, A., Wagner, P. E., Walther, H., Weingartner, E., Wex, H., Winkler, P. M., Carslaw, K. S., Worsnop, D. R., Baltensperger, U., and Kulmala, M.: Role of sulphuric acid, ammonia and galactic cosmic rays in atmospheric aerosol nucleation, Nature, 476, 429–433, https://doi.org/10.1038/nature10343, 2011.

https://doi.org/10.5194/egusphere-2026-4542
Preprint. Discussion started: 16 September 2026

Kirkby, J., Duplissy, J., Sengupta, K., Frege, C., Gordon, H., Williamson, C., Heinritzi, M., Simon, M., Yan, C., Almeida, J., Tröstl, J., Nieminen, T., Ortega, I. K., Wagner, R., Adamov, A., Amorim, A., Bernhammer, A.-K., Bianchi, F., Breitenlechner, M., Brilke, S., Chen, X., Craven, J., Dias, A., Ehrhart, S., Flagan, R. C., Franchin, A., Fuchs, C., Guida, R., Hakala, J., Hoyle, C. R., Jokinen, T., Junninen, H., Kangasluoma, J., Kim, J., Krapf, M., Kürten, A., Laaksonen, A., Lehtipalo, K., Makhmutov, V., Mathot, S., Molteni, U., Onnela, A., Peräkylä, O., Piel, F., Petäjä, T., Praplan, A. P., Pringle, K., Rap, A., Richards, N. A. D., Riipinen, I., Rissanen, M. P., Rondo, L., Sarnela, N., Schobesberger, S., Scott, C. E., Seinfeld, J. H., Sipilä, M., Steiner, G., Stozhkov, Y., Stratmann, F., Tomé, A., Virtanen, A., Vogel, A. L., Wagner, A. C., Wagner, P. E., Weingartner, E., Wimmer, D., Winkler, P. M., Ye, P., Zhang, X., Hansel, A., Dommen, J., Donahue, N. M., Worsnop, D. R., Baltensperger, U., Kulmala, M., Carslaw, K. S., and Curtius, J.: Ion-induced nucleation of pure biogenic particles, Nature, 533, 521–526, https://doi.org/10.1038/nature17953, 2016.

Kiyoura, R. and Urano, K.: Mechanism, Kinetics, and Equilibrium of Thermal Decomposition of Ammonium Sulfate, Industrial & Engineering Chemistry Process Design and Development, 9, 489–494, https://doi.org/10.1021/i260036a001, publisher: American Chemical Society (ACS), 1970.

Kortüm, G., Vogel, W., and Andrussow, K.: Dissociation constants of organic acids in aqueous solution, 1961.

Krieger, U. K., Siegrist, F., Marcolli, C., Emanuelsson, E. U., Gøbel, F. M., Bilde, M., Marsh, A., Reid, J. P., Huisman, A. J., Riipinen, I., Hyttinen, N., Myllys, N., Kurtén, T., Bannan, T., Percival, C. J., and Topping, D.: A reference data set for validating vapor pressure measurement techniques: homologous series of polyethylene glycols, Atmospheric Measurement Techniques, 11, 49–63, https://doi.org/10.5194/amt-11-49-2018, 2018.

Krüger, M., Galeazzo, T., Eremets, I., Schmidt, B., Pöschl, U., Shiraiwa, M., and Berkemeier, T.: Improved vapor pressure predictions using group contribution-assisted graph convolutional neural networks (GC^2 NN), Geoscientific Model Development, 18, 7357–7371, https://doi.org/10.5194/gmd-18-7357-2025, 2025.

Kulmala, M. and Laaksonen, A.: Binary nucleation of water–sulfuric acid system: Comparison of classical theories with different H2SO4 saturation vapor pressures, The Journal of Chemical Physics, 93, 696–701, https://doi.org/10.1063/1.459519, 1990.

Kurtén, T., Tiusanen, K., Roldin, P., Rissanen, M., Luy, J.-N., Boy, M., Ehn, M., and Donahue, N.: α-Pinene Autoxidation Products May Not Have Extremely Low Saturation Vapor Pressures Despite High O:C Ratios, The Journal of Physical Chemistry A, 120, 2569–2582, https://doi.org/10.1021/acs.jpca.6b02196, 2016.

Lange, N. A. and Dean, J. A.: Lange's Handbook of Chemistry, McGraw-Hill, New York St. Louis San Francisco [etc.], 15th ed edn., ISBN 978-0-07-016384-3, 1998.

Le Breton, M., Wang, Y., Hallquist, M., Pathak, R. K., Zheng, J., Yang, Y., Shang, D., Glasius, M., Bannan, T. J., Liu, Q., Chan, C. K., Percival, C. J., Zhu, W., Lou, S., Topping, D., Wang, Y., Yu, J., Lu, K., Guo, S., Hu, M., and Hallquist, M.: Online gas- and particle-phase measurements of organosulfates, organosulfonates and nitrooxy organosulfates in Beijing utilizing a FIGAERO ToF-CIMS, Atmospheric Chemistry and Physics, 18, 10 355–10 371, https://doi.org/10.5194/acp-18-10355-2018, 2018.

Lee, A. K. Y., Hayden, K. L., Herckes, P., Leaitch, W. R., Liggio, J., Macdonald, A. M., and Abbatt, J. P. D.: Characterization of aerosol and cloud water at a mountain site during WACS 2010: secondary organic aerosol formation through oxidative cloud processing, Atmospheric Chemistry and Physics, 12, 7103–7116, https://doi.org/10.5194/acp-12-7103-2012, 2012.

Longnecker, E. R., Bakker-Arkema, J. G., and Ziemann, P. J.: Comparison of Vapor Pressure Estimation Methods Used to Model Secondary Organic Aerosol Formation from Reactions of Linear and Branched Alkenes with OH/NO_x, ACS Earth and Space Chemistry, 9, 314–326, https://doi.org/10.1021/acsearthspacechem.4c00285, 2025.

https://doi.org/10.5194/egusphere-2026-4542
Preprint. Discussion started: 16 September 2026

Lopez, B., Bhattacharyya, N., DeVivo, J., Wang, M., Caudillo-Plath, L., Surdu, M., Bianchi, F., Brasseur, Z., Buchholz, A., Chen, D., Duplissy, J., He, X.-C., Hofbauer, V., Mahfouz, N., Makhmutov, V., Marten, R., Mentler, B., Philippov, M., Schervish, M., Wang, D. S., Weber, S. K., Welti, A., El Haddad, I., Lehtipalo, K., Kulmala, M., Worsnop, D., Kirkby, J., Mauldin, R. L., Stolzenburg, D., Schobesberger, S., Flagan, R., and Donahue, N. M.: A diagonal volatility basis set to assess the condensation of organic vapors onto particles, Environmental Science: Atmospheres, 5, 1035–1061, https://doi.org/10.1039/D5EA00062A, 2025.

Lopez-Hilfiker, F. D., Mohr, C., Ehn, M., Rubach, F., Kleist, E., Wildt, J., Mentel, T. F., Lutz, A., Hallquist, M., Worsnop, D., and Thornton, J. A.: A novel method for online analysis of gas and particle composition: description and evaluation of a Filter Inlet for Gases and AEROsols (FIGAERO), Atmospheric Measurement Techniques, 7, 983–1001, https://doi.org/10.5194/amt-7-983-2014, 2014.

Lopez-Hilfiker, F. D., Mohr, C., Ehn, M., Rubach, F., Kleist, E., Wildt, J., Mentel, T. F., Carrasquillo, A. J., Daumit, K. E., Hunter, J. F., Kroll, J. H., Worsnop, D. R., and Thornton, J. A.: Phase partitioning and volatility of secondary organic aerosol components formed from α-pinene ozonolysis and OH oxidation: the importance of accretion products and other low volatility compounds, Atmospheric Chemistry and Physics, 15, 7765–7776, https://doi.org/10.5194/acp-15-7765-2015, 2015.

Lopez-Hilfiker, F. D., Mohr, C., D'Ambro, E. L., Lutz, A., Riedel, T. P., Gaston, C. J., Iyer, S., Zhang, Z., Gold, A., Surratt, J. D., Lee, B. H., Kurten, T., Hu, W., Jimenez, J., Hallquist, M., and Thornton, J. A.: Molecular Composition and Volatility of Organic Aerosol in the Southeastern U.S.: Implications for IEPOX Derived SOA, Environmental Science & Technology, 50, 2200–2209, https://doi.org/10.1021/acs.est.5b04769, 2016.

Lutz, A., Mohr, C., Le Breton, M., Lopez-Hilfiker, F. D., Priestley, M., Thornton, J. A., and Hallquist, M.: Gas to Particle Partitioning of Organic Acids in the Boreal Atmosphere, ACS Earth and Space Chemistry, 3, 1279–1287, https://doi.org/10.1021/acsearthspacechem.9b00041, 2019.

Ma, J., Reininger, N., Zhao, C., Döbler, D., Rüdiger, J., Qiu, Y., Ungeheuer, F., Simon, M., D'Angelo, L., Breuninger, A., David, J., Bai, Y., Li, Y., Xue, Y., Li, L., Wang, Y., Hildmann, S., Hoffmann, T., Liu, B., Niu, H., Wu, Z., and Vogel, A. L.: Unveiling a large fraction of hidden organosulfates in ambient organic aerosol, Nature Communications, 16, 4098, https://doi.org/10.1038/s41467-025-59420-y, 2025.

Marti, J. J., Jefferson, A., Cai, X. P., Richert, C., McMurry, P. H., and Eisele, F.: H_2 SO_4 vapor pressure of sulfuric acid and ammonium sulfate solutions, Journal of Geophysical Research: Atmospheres, 102, 3725–3735, https://doi.org/10.1029/96JD03064, 1997.

Mauldin, R. L., Tanner, D. J., Heath, J. A., Huebert, B. J., and Eisele, F. L.: Observations of H_2 SO_4 and MSA during PEM-Tropics-A, Journal of Geophysical Research: Atmospheres, 104, 5801–5816, https://doi.org/10.1029/98JD02612, 1999.

McManus, J. B., Zahniser, M. S., Nelson, D. D., Shorter, J. H., Herndon, S. C., Jervis, D., Agnese, M., McGovern, R., Yacovitch, T. I., and Roscioli, J. R.: Recent progress in laser-based trace gas instruments: performance and noise analysis, Applied Physics B, 119, 203–218, https://doi.org/10.1007/s00340-015-6033-0, 2015.

McNeill, V. F., Wolfe, G. M., and Thornton, J. A.: The Oxidation of Oleate in Submicron Aqueous Salt Aerosols: Evidence of a Surface Process, The Journal of Physical Chemistry A, 111, 1073–1083, https://doi.org/10.1021/jp066233f, 2007.

Miljevic, B., Mallet, M. D., Osuagwu, C. G., Ristovski, Z. D., Humphries, R. S., Selleck, P., Taylor, S., and Keywood, M. D.: Aerosol acidity controls methanesulfonic acid evaporation from aerosols during Antarctic katabatic outflow, Communications Earth & Environment, 6, 1057, https://doi.org/10.1038/s43247-025-03041-2, 2025.

Nannoolal, Y., Rarey, J., and Ramjugernath, D.: Estimation of pure component properties, Fluid Phase Equilibria, 269, 117–133, https://doi.org/10.1016/j.fluid.2008.04.020, 2008.

https://doi.org/10.5194/egusphere-2026-4542
Preprint. Discussion started: 16 September 2026

Pankow, J. F. and Asher, W. E.: SIMPOL.1: a simple group contribution method for predicting vapor pressures and enthalpies of vaporization of multifunctional organic compounds, Atmospheric Chemistry and Physics, 8, 2773–2796, https://doi.org/10.5194/acp-8-2773-2008, 2008.

Riva, M., Pospisilova, V., Frege, C., Perrier, S., Bansal, P., Jorga, S., Sturm, P., Thornton, J. A., Rohner, U., and Lopez-Hilfiker, F.: Evaluation of a reduced-pressure chemical ion reactor utilizing adduct ionization for the detection of gaseous organic and inorganic species, Atmospheric Measurement Techniques, 17, 5887–5901, https://doi.org/10.5194/amt-17-5887-2024, 2024.

Rumble, R. ed., J.: Physical Constants of Organic Compounds, in: CRC Handbook of Chemistry and Physics, 106th Edition (Internet Version 2025), CRC press/Taylor & Francis Boca Raton, FL, 2025.

Schervish, M., Heinritzi, M., Stolzenburg, D., Dada, L., Wang, M., Ye, Q., Hofbauer, V., DeVivo, J., Bianchi, F., Brilke, S., Duplissy, J., El Haddad, I., Finkenzeller, H., He, X.-C., Kvashnin, A., Kim, C., Kirkby, J., Kulmala, M., Lehtipalo, K., Lopez, B., Makhmutov, V., Mentler, B., Molteni, U., Nie, W., Petäjä, T., Quéléver, L., Volkamer, R., Wagner, A. C., Winkler, P., Yan, C., and Donahue, N. M.: Interactions of peroxy radicals from monoterpene and isoprene oxidation simulated in the radical volatility basis set, Environmental Science: Atmospheres, 4, 740–753, https://doi.org/10.1039/D4EA00056K, 2024.

Schobesberger, S., Franchin, A., Bianchi, F., Rondo, L., Duplissy, J., Kürten, A., Ortega, I. K., Metzger, A., Schnitzhofer, R., Almeida, J., Amorim, A., Dommen, J., Dunne, E. M., Ehn, M., Gagné, S., Ickes, L., Junninen, H., Hansel, A., Kerminen, V.-M., Kirkby, J., Kupc, A., Laaksonen, A., Lehtipalo, K., Mathot, S., Onnela, A., Petäjä, T., Riccobono, F., Santos, F. D., Sipilä, M., Tomé, A., Tsagkogeorgas, G., Viisanen, Y., Wagner, P. E., Wimmer, D., Curtius, J., Donahue, N. M., Baltensperger, U., Kulmala, M., and Worsnop, D. R.: On the composition of ammonia–sulfuric-acid ion clusters during aerosol particle formation, Atmospheric Chemistry and Physics, 15, 55–78, https://doi.org/10.5194/acp-15-55-2015, 2015.

Schobesberger, S., D'Ambro, E. L., Lopez-Hilfiker, F. D., Mohr, C., and Thornton, J. A.: A model framework to retrieve thermodynamic and kinetic properties of organic aerosol from composition-resolved thermal desorption measurements, Atmospheric Chemistry and Physics, 18, 14 757–14 785, https://doi.org/10.5194/acp-18-14757-2018, 2018.

Scott, W. and Cattell, F.: Vapor pressure of ammonium sulfates, Atmospheric Environment (1967), 13, 307–317, https://doi.org/10.1016/0004-6981(79)90174-4, publisher: Elsevier BV, 1979.

Serjeant, E. P. and Dempsey, B.: Ionisation constants of organic acids in aqueous solution, no. 23 in IUPAC chemical data series, Pergamon Press, Oxford, ISBN 978-0-08-022339-1, 1979.

Shen, J., Russell, D. M., DeVivo, J., Kunkler, F., Baalbaki, R., Mentler, B., Scholz, W., Yu, W., Caudillo-Plath, L., Sommer, E., Ahongshangbam, E., Alfaouri, D., Almeida, J., Amorim, A., Beck, L. J., Beckmann, H., Berntheusel, M., Bhattacharyya, N., Canagaratna, M. R., Chassaing, A., Cruz-Simbron, R., Dada, L., Duplissy, J., Gordon, H., Granzin, M., Große Schute, L., Heinritzi, M., Iyer, S., Klebach, H., Krüger, T., Kürten, A., Lampimäki, M., Liu, L., Lopez, B., Martinez, M., Morawiec, A., Onnela, A., Peltola, M., Rato, P., Reza, M., Richter, S., Rörup, B., Kaniyodical Sebastian, M., Simon, M., Surdu, M., Tamme, K., Thakur, R. C., Tomé, A., Tong, Y., Top, J., Umo, N. S., Unfer, G., Vettikkat, L., Weissbacher, J., Xenofontos, C., Yang, B., Zauner-Wieczorek, M., Zhang, J., Zheng, Z., Baltensperger, U., Christoudias, T., Flagan, R. C., El Haddad, I., Junninen, H., Möhler, O., Riipinen, I., Rohner, U., Schobesberger, S., Volkamer, R., Winkler, P. M., Hansel, A., Lehtipalo, K., Donahue, N. M., Lelieveld, J., Harder, H., Kulmala, M., Worsnop, D. R., Kirkby, J., Curtius, J., and He, X.-C.: New particle formation from isoprene under upper-tropospheric conditions: data sources, https://doi.org/10.5281/ZENODO.12635638, 2024.

https://doi.org/10.5194/egusphere-2026-4542
Preprint. Discussion started: 16 September 2026

Siegel, K., Karlsson, L., Zieger, P., Baccarini, A., Schmale, J., Lawler, M., Salter, M., Leck, C., Ekman, A. M. L., Riipinen, I., and Mohr, C.: Insights into the molecular composition of semi-volatile aerosols in the summertime central Arctic Ocean using FIGAERO-CIMS, Environmental Science: Atmospheres, 1, 161–175, https://doi.org/10.1039/D0EA00023J, 2021.

Stark, H., Yatavelli, R. L. N., Thompson, S. L., Kang, H., Krechmer, J. E., Kimmel, J. R., Palm, B. B., Hu, W., Hayes, P. L., Day, D. A., Campuzano-Jost, P., Canagaratna, M. R., Jayne, J. T., Worsnop, D. R., and Jimenez, J. L.: Impact of Thermal Decomposition on Thermal Desorption Instruments: Advantage of Thermogram Analysis for Quantifying Volatility Distributions of Organic Species, Environmental Science & Technology, 51, 8491–8500, https://doi.org/10.1021/acs.est.7b00160, 2017.

Stolzenburg, D., Fischer, L., Vogel, A. L., Heinritzi, M., Schervish, M., Simon, M., Wagner, A. C., Dada, L., Ahonen, L. R., Amorim, A., Baccarini, A., Bauer, P. S., Baumgartner, B., Bergen, A., Bianchi, F., Breitenlechner, M., Brilke, S., Buenrostro Mazon, S., Chen, D., Dias, A., Draper, D. C., Duplissy, J., El Haddad, I., Finkenzeller, H., Frege, C., Fuchs, C., Garmash, O., Gordon, H., He, X., Helm, J., Hofbauer, V., Hoyle, C. R., Kim, C., Kirkby, J., Kontkanen, J., Kürten, A., Lampilahti, J., Lawler, M., Lehtipalo, K., Leiminger, M., Mai, H., Mathot, S., Mentler, B., Molteni, U., Nie, W., Nieminen, T., Nowak, J. B., Ojdanic, A., Onnela, A., Passananti, M., Petäjä, T., Quéléver, L. L. J., Rissanen, M. P., Sarnela, N., Schallhart, S., Tauber, C., Tomé, A., Wagner, R., Wang, M., Weitz, L., Wimmer, D., Xiao, M., Yan, C., Ye, P., Zha, Q., Baltensperger, U., Curtius, J., Dommen, J., Flagan, R. C., Kulmala, M., Smith, J. N., Worsnop, D. R., Hansel, A., Donahue, N. M., and Winkler, P. M.: Rapid growth of organic aerosol nanoparticles over a wide tropospheric temperature range, Proceedings of the National Academy of Sciences, 115, 9122–9127, https://doi.org/10.1073/pnas.1807604115, 2018.

Stolzenburg, D., Simon, M., Ranjithkumar, A., Kürten, A., Lehtipalo, K., Gordon, H., Ehrhart, S., Finkenzeller, H., Pichelstorfer, L., Nieminen, T., He, X.-C., Brilke, S., Xiao, M., Amorim, A., Baalbaki, R., Baccarini, A., Beck, L., Bräkling, S., Caudillo Murillo, L., Chen, D., Chu, B., Dada, L., Dias, A., Dommen, J., Duplissy, J., El Haddad, I., Fischer, L., Gonzalez Carracedo, L., Heinritzi, M., Kim, C., Koenig, T. K., Kong, W., Lamkaddam, H., Lee, C. P., Leiminger, M., Li, Z., Makhmutov, V., Manninen, H. E., Marie, G., Marten, R., Müller, T., Nie, W., Partoll, E., Petäjä, T., Pfeifer, J., Philippov, M., Rissanen, M. P., Rörup, B., Schobesberger, S., Schuchmann, S., Shen, J., Sipilä, M., Steiner, G., Stozhkov, Y., Tauber, C., Tham, Y. J., Tomé, A., Vazquez-Pufleau, M., Wagner, A. C., Wang, M., Wang, Y., Weber, S. K., Wimmer, D., Wlasits, P. J., Wu, Y., Ye, Q., Zauner-Wieczorek, M., Baltensperger, U., Carslaw, K. S., Curtius, J., Donahue, N. M., Flagan, R. C., Hansel, A., Kulmala, M., Lelieveld, J., Volkamer, R., Kirkby, J., and Winkler, P. M.: Enhanced growth rate of atmospheric particles from sulfuric acid, Atmospheric Chemistry and Physics, 20, 7359–7372, https://doi.org/10.5194/acp-20-7359-2020, 2020.

Thornton, J. A., Mohr, C., Schobesberger, S., D'Ambro, E. L., Lee, B. H., and Lopez-Hilfiker, F. D.: Evaluating Organic Aerosol Sources and Evolution with a Combined Molecular Composition and Volatility Framework Using the Filter Inlet for Gases and Aerosols (FIGAERO), Accounts of Chemical Research, 53, 1415–1426, https://doi.org/10.1021/acs.accounts.0c00259, publisher: American Chemical Society (ACS), 2020.

Toivola, M., Prisle, N. L., Elm, J., Waxman, E. M., Volkamer, R., and Kurtén, T.: Can COSMOTherm Predict a Salting in Effect?, The Journal of Physical Chemistry A, 121, 6288–6295, https://doi.org/10.1021/acs.jpca.7b04847, 2017.

Ullrich, R., Hoose, C., Möhler, O., Niemand, M., Wagner, R., Höhler, K., Hiranuma, N., Saathoff, H., and Leisner, T.: A New Ice Nucleation Active Site Parameterization for Desert Dust and Soot, Journal of the Atmospheric Sciences, 74, 699–717, https://doi.org/10.1175/JAS-D-16-0074.1, 2017.

Voisin, D., Smith, J. N., Sakurai, H., McMurry, P. H., and Eisele, F. L.: Thermal Desorption Chemical Ionization Mass Spectrometer for Ultrafine Particle Chemical Composition, Aerosol Science and Technology, 37, 471–475, https://doi.org/10.1080/02786820300959, 2003.

https://doi.org/10.5194/egusphere-2026-4542
Preprint. Discussion started: 16 September 2026

Wakeen, J., O'Donnell, S. E., Collins, D. R., Pierce, J. R., and Smith, J. N.: Positive matrix factorization reveals volatility-resolved composition from new particle formation during α-pinene ozonolysis, Aerosol Science and Technology, pp. 1–17, https://doi.org/10.1080/02786826.2026.2649824, 2026.

Wang, M., Kong, W., Marten, R., He, X.-C., Chen, D., Pfeifer, J., Heitto, A., Kontkanen, J., Dada, L., Kürten, A., Yli-Juuti, T., Manninen, H. E., Amanatidis, S., Amorim, A., Baalbaki, R., Baccarini, A., Bell, D. M., Bertozzi, B., Bräkling, S., Brilke, S., Murillo, L. C., Chiu, R., Chu, B., De Menezes, L.-P., Duplissy, J., Finkenzeller, H., Carracedo, L. G., Granzin, M., Guida, R., Hansel, A., Hofbauer, V., Krechmer, J., Lehtipalo, K., Lamkaddam, H., Lampimäki, M., Lee, C. P., Makhmutov, V., Marie, G., Mathot, S., Mauldin, R. L., Mentler, B., Müller, T., Onnela, A., Partoll, E., Petäjä, T., Philippov, M., Pospisilova, V., Ranjithkumar, A., Rissanen, M., Rörup, B., Scholz, W., Shen, J., Simon, M., Sipilä, M., Steiner, G., Stolzenburg, D., Tham, Y. J., Tomé, A., Wagner, A. C., Wang, D. S., Wang, Y., Weber, S. K., Winkler, P. M., Wlasits, P. J., Wu, Y., Xiao, M., Ye, Q., Zauner-Wieczorek, M., Zhou, X., Volkamer, R., Riipinen, I., Dommen, J., Curtius, J., Baltensperger, U., Kulmala, M., Worsnop, D. R., Kirkby, J., Seinfeld, J. H., El-Haddad, I., Flagan, R. C., and Donahue, N. M.: Rapid growth of new atmospheric particles by nitric acid and ammonia condensation, Nature, 581, 184–189, https://doi.org/10.1038/s41586-020-2270-4, 2020.

Wang, M., He, X.-C., Finkenzeller, H., Iyer, S., Chen, D., Shen, J., Simon, M., Hofbauer, V., Kirkby, J., Curtius, J., Maier, N., Kurtén, T., Worsnop, D. R., Kulmala, M., Rissanen, M., Volkamer, R., Tham, Y. J., Donahue, N. M., and Sipilä, M.: Measurement of iodine species and sulfuric acid using bromide chemical ionization mass spectrometers, Atmospheric Measurement Techniques, 14, 4187–4202, https://doi.org/10.5194/amt-14-4187-2021, 2021.

Wang, M., Xiao, M., Bertozzi, B., Marie, G., Rörup, B., Schulze, B., Bardakov, R., He, X.-C., Shen, J., Scholz, W., Marten, R., Dada, L., Baalbaki, R., Lopez, B., Lamkaddam, H., Manninen, H. E., Amorim, A., Ataei, F., Bogert, P., Brasseur, Z., Caudillo, L., De Menezes, L.-P., Duplissy, J., Ekman, A. M. L., Finkenzeller, H., Carracedo, L. G., Granzin, M., Guida, R., Heinritzi, M., Hofbauer, V., Höhler, K., Korhonen, K., Krechmer, J. E., Kürten, A., Lehtipalo, K., Mahfouz, N. G. A., Makhmutov, V., Massabò, D., Mathot, S., Mauldin, R. L., Mentler, B., Müller, T., Onnela, A., Petäjä, T., Philippov, M., Piedehierro, A. A., Pozzer, A., Ranjithkumar, A., Schervish, M., Schobesberger, S., Simon, M., Stozhkov, Y., Tomé, A., Umo, N. S., Vogel, F., Wagner, R., Wang, D. S., Weber, S. K., Welti, A., Wu, Y., Zauner-Wieczorek, M., Sipilä, M., Winkler, P. M., Hansel, A., Baltensperger, U., Kulmala, M., Flagan, R. C., Curtius, J., Riipinen, I., Gordon, H., Lelieveld, J., El-Haddad, I., Volkamer, R., Worsnop, D. R., Christoudias, T., Kirkby, J., Möhler, O., and Donahue, N. M.: Synergistic HNO3–H2SO4–NH3 upper tropospheric particle formation, Nature, 605, 483–489, https://doi.org/10.1038/s41586-022-04605-4, 2022.

Warneck, P.: In-cloud chemistry opens pathway to the formation of oxalic acid in the marine atmosphere, Atmospheric Environment, 37, 2423–2427, https://doi.org/10.1016/S1352-2310(03)00136-5, 2003.

West, C. P., Hsu, Y.-J., MacFeely, K. T., Huston, S. M., Aridjis-Olivos, B. P., Morales, A. C., and Laskin, A.: Volatility Measurements of Individual Components in Organic Aerosol Mixtures Using Temperature-Programmed Desorption–Direct Analysis in Real Time–High Resolution Mass Spectrometry, Analytical Chemistry, 95, 7403–7408, https://doi.org/10.1021/acs.analchem.3c00923, publisher: American Chemical Society (ACS), 2023.

Xie, Q., Smith, A. M., Botero-Carrizosa, S. C., Sharpe, S. A. L., Dekel, G., June, N. A., Shrivastava, M., Dai, Y., Ridgway, K., L'Orange, C., Jathar, S. H., Hopstock, K. S., Nizkorodov, S. A., Rudich, Y., and Laskin, A.: Matrix effects reshape organic aerosol volatility and atmospheric persistence, Proceedings of the National Academy of Sciences, 123, e2614944 123, https://doi.org/10.1073/pnas.2614944123, 2026.

https://doi.org/10.5194/egusphere-2026-4542
Preprint. Discussion started: 16 September 2026

Yang, L. H., Takeuchi, M., Chen, Y., and Ng, N. L.: Characterization of thermal decomposition of oxygenated organic compounds in FIGAERO-CIMS, Aerosol Science and Technology, 55, 1321–1342, https://doi.org/10.1080/02786826.2021.1945529, 2021.

Yaws, C. L.: Handbook of Vapor Pressure, v. 4: Library of physico-chemical property data, Gulf Pub. Co, Houston, ISBN 978-0-88415-189-0 978-0-88415-190-6 978-0-88415-191-3 978-0-88415-394-8, 1994.

Ye, C., Yuan, B., Lin, Y., Wang, Z., Hu, W., Li, T., Chen, W., Wu, C., Wang, C., Huang, S., Qi, J., Wang, B., Wang, C., Song, W., Wang, X., Zheng, E., Krechmer, J. E., Ye, P., Zhang, Z., Wang, X., Worsnop, D. R., and Shao, M.: Chemical characterization of oxygenated organic compounds in the gas phase and particle phase using iodide CIMS with FIGAERO in urban air, Atmospheric Chemistry and Physics, 21, 8455–8478, https://doi.org/10.5194/acp-21-8455-2021, 2021.

Ye, Q., Wang, M., Hofbauer, V., Stolzenburg, D., Chen, D., Schervish, M., Vogel, A., Mauldin, R. L., Baalbaki, R., Brilke, S., Dada, L., Dias, A., Duplissy, J., El Haddad, I., Finkenzeller, H., Fischer, L., He, X., Kim, C., Kürten, A., Lamkaddam, H., Lee, C. P., Lehtipalo, K., Leiminger, M., Manninen, H. E., Marten, R., Mentler, B., Partoll, E., Petäjä, T., Rissanen, M., Schobesberger, S., Schuchmann, S., Simon, M., Tham, Y. J., Vazquez-Pufleau, M., Wagner, A. C., Wang, Y., Wu, Y., Xiao, M., Baltensperger, U., Curtius, J., Flagan, R., Kirkby, J., Kulmala, M., Volkamer, R., Winkler, P. M., Worsnop, D., and Donahue, N. M.: Molecular Composition and Volatility of Nucleated Particles from α-Pinene Oxidation between -50 °C and +25 °C, Environmental Science & Technology, 53, 12 357–12 365, https://doi.org/10.1021/acs.est.9b03265, 2019.

Ylisirniö, A., Barreira, L. M. F., Pullinen, I., Buchholz, A., Jayne, J., Krechmer, J. E., Worsnop, D. R., Virtanen, A., and Schobesberger, S.: On the calibration of FIGAERO-ToF-CIMS: importance and impact of calibrant delivery for the particle-phase calibration, Atmospheric Measurement Techniques, 14, 355–367, https://doi.org/10.5194/amt-14-355-2021, 2021.

Ylisirniö, A., Hyttinen, N., Li, Z., Alton, M., Nissinen, A., Pullinen, I., Miettinen, P., Yli-Juuti, T., and Schobesberger, S.: The saturation vapor pressures of higher-order polyethylene glycols and achieving a wide calibration range for volatility measurements by FIGAERO-CIMS, Atmospheric Measurement Techniques, 18, 6449–6464, https://doi.org/10.5194/amt-18-6449-2025, 2025.

Yu, W., Baalbaki, R., Shen, J., DeVivo, J., Caudillo-Plath, L., Sommer, E., Heitto, A., Klebach, H., Russell, D. M., Amorim, A., Beckmann, H., Bhattacharyya, N., Blankenship, V., Chassaing, A., Cruz-Simbron, R., Dada, L., Jacobshagen, A., Judmaier, B., Kaniyodical Sebastian, M., Konrat, R., Krüger, T., Kunkler, F., Lietzke, C. J., Liu, L., Mauldin, R., Mentler, B., Morawiec, A., Rato, P., Rörup, B., Ruhl, S., Scholz, W., Simon, M., Stinchfield, A., Tomé, A., Tong, Y., Top, J., Umo, N. S., Unfer, G. R., Vettikkat, L., Weissbacher, J., Xenofontos, C., Yang, B., Zauner-Wieczorek, M., Zhang, J., Zheng, Z., Christoudias, T., Curtius, J., El Haddad, I., Flagan, R., Hansel, A., Harder, H., Kürten, A., Möhler, O., Petäjä, T., Volkamer, R., Winkler, P. M., Worsnop, D. R., Kulmala, M., Donahue, N. M., Kirkby, J., Yli-Juuti, T., Riipinen, I., He, X.-C., and Lehtipalo, K.: Impact of humidity on aerosol growth from methanesulfonic acid, Environmental Science: Atmospheres, p. 10.1039.D5EA00123D, https://doi.org/10.1039/D5EA00123D, 2026.

Zelenková, G. and Slovák, V.: Decomposition of ammonium salts by quantitative TG-MS, Journal of Thermal Analysis and Calorimetry, 147, 15 059–15 068, https://doi.org/10.1007/s10973-022-11747-0, 2022.

Zhang, Q., Jimenez, J. L., Worsnop, D. R., and Canagaratna, M.: A Case Study of Urban Particle Acidity and Its Influence on Secondary Organic Aerosol, Environmental Science & Technology, 41, 3213–3219, https://doi.org/10.1021/es061812j, 2007.

Zhang, R., Li, Y., Zhao, J., Aridjis-Olivos, B., Zhao, L., Kowalewski, V., Kabir, M., Johnson, N. M., Nielsen, E. R., Brooks, S. D., Zhang, Y., Vedlitz, A., Porter, W., North, S. W., Li, W., Young, M. W., Seinfeld, J. H., Wang, Y., and Wang, Y.: Detecting supramolecular organic nanoparticles during heat wave, Science, 391, eady5192, https://doi.org/10.1126/science.ady5192, 2026.

Zhao, B., Donahue, N. M., Zhang, K., Mao, L., Shrivastava, M., Ma, P.-L., Shen, J., Wang, S., Sun, J., Gordon, H., Tang, S., Fast, J., Wang, M., Gao, Y., Yan, C., Singh, B., Li, Z., Huang, L., Lou, S., Lin, G., Wang, H., Jiang, J., Ding, A., Nie, W., Qi, X., Chi, X., and Wang, L.:

https://doi.org/10.5194/egusphere-2026-4542
Preprint. Discussion started: 16 September 2026

Global variability in atmospheric new particle formation mechanisms, Nature, 631, 98–105, https://doi.org/10.1038/s41586-024-07547-1, 2024.

Zhao, Y., Kreisberg, N. M., Worton, D. R., Isaacman, G., Weber, R. J., Liu, S., Day, D. A., Russell, L. M., Markovic, M. Z., VandenBoer, T. C., Murphy, J. G., Hering, S. V., and Goldstein, A. H.: Insights into Secondary Organic Aerosol Formation Mechanisms from Measured Gas/Particle Partitioning of Specific Organic Tracer Compounds, Environmental Science & Technology, 47, 3781–3787, https://doi.org/10.1021/es304587x, 2013.